

Article

Mineralogy and Genesis of the Kihabe Zn-Pb-V Prospect, Aha Hills, Northwest Botswana

Nicola Mondillo ^{1,2,*}, Maria Boni ^{1,2}, Giuseppina Balassone ¹, Nigel Forrester ³,
Francesco Putzolu ¹  and Licia Santoro ²

¹ Dipartimento di Scienze della Terra, dell'Ambiente e delle Risorse, Università degli Studi di Napoli Federico II, 80126 Napoli, Italy; boni@unina.it (M.B.); balasson@unina.it (G.B.); francesco.putzolu@unina.it (F.P.)

² Earth Sciences Department, Natural History Museum, Cromwell Road, London SW7 5BD, UK; licia.santoro85@gmail.com

³ Mount Burgess Mining N.L., East Victoria Park 6101, Australia; Nigel@mountburgess.com

* Correspondence: nicola.mondillo@unina.it

Received: 26 June 2020; Accepted: 27 July 2020; Published: 31 July 2020



Abstract: The Kihabe Zn-Pb-V > (Cu-Ag-Ge) prospect is located at the boundary between Namibia and Botswana (Aha Hills, Ngamiland District) in a strongly deformed Proterozoic fold belt, corresponding to the NE extension of the Namibian Damara Orogen. The Kihabe prospect contains Zn-Pb resources of 14.4 million tonnes at 2.84% zinc equivalent, Ag resources of 3.3 million ounces, and notable V-Ge amounts, still not evaluated at a resource level. The ores are represented by a mixed sulfide–nonsulfide mineralization. Sulfide minerals consist mainly of sphalerite, galena and pyrite in a metamorphic quartzwacke. Among the nonsulfide assemblage, two styles of mineralization occur in the investigated samples: A first one, characterized by hydrothermal willemite and baileychlore, and a second one consisting of supergene smithsonite, cerussite, hemimorphite, Pb-phosphates, arsenates and vanadates. Willemite is present in two generations, which postdate sulfide emplacement and may also form at their expenses. These characteristics are similar to those observed in the willemite occurrences of the nearby Otavi Mountainland, which formed through hydrothermal processes, during the final stages of the Damara Orogeny. The formation of the Kihabe willemite is likely coeval. Baileychlore is characterized by textures indicating direct precipitation from solutions and dissolution–crystallization mechanisms. Both processes are typical of hydrothermal systems, thus suggesting a hydrothermal genesis for the Kihabe Zn-chlorite as well. Baileychlore could represent an alteration halo possibly associated either with the sulfide or with willemite mineralization. The other nonsulfide minerals, smithsonite, cerussite, various Pb-phosphates and vanadates, are clearly genetically associated with late phases of supergene alteration, which overprinted both the sulfide and the willemite- and baileychlore-bearing mineralizations. Supergene alteration probably occurred in this part of Botswana from the Late Cretaceous to the Miocene.

Keywords: Botswana; Aha Hills; sulfides; nonsulfides; willemite; baileychlore; chlorite; smithsonite

1. Introduction

Mineral exploration and mining in Botswana has been historically dominated by diamonds and, to lesser extent, by base metals. Copper, gold and nickel have held significant, though smaller, roles in the economy [1]. In particular, after the early 2000s, exploration for Cu-Ag deposits intensified in western parts of Botswana, in the so-called Kalahari Copper Belt (KCB) [1]. Among the various metallogenic regions of the country, the only zone currently showing mineral potential for polymetallic Zn-Pb-Cu-Ag-V-Ge is in northwest Botswana, which represents the northeastern extension of the Namibian Damara Belt [1] (Figures 1 and 2). This is because the Damara Belt of the nearby Otavi

Mountainland (OML) in Namibia is host to several base metal ore deposits [2]. These deposits can be grouped into at least four ore types: (1) Berg Aukas-type Zn-Pb deposits in carbonates; (2) Tsumeb-type Pb-Cu-Zn-Ge deposits in carbonates; (3) Abenab-type vanadium deposits in geologically young karst pipes and breccias; and (4) Tschudi-type low-grade Cu ores in sandstone and conglomerates of the basal Mulden Group [3]. Among these, the Berg Aukas- and Tsumeb-types, both hosted by carbonate rocks of the Otavi Group, are the economically most important mineral deposits. Berg Aukas-type deposits are considered to have formed either before the Pan-African Orogeny (as Mississippi Valley-type MVT mineralization [4,5]) or during the Pan-African Orogeny [6]. Tsumeb-type deposits should instead derive from hydrothermal fluids generated during prograde metamorphism of the Pan-African Orogeny, which migrated along Pan-African faults, forming Pb-Cu-Ge-sulfide ores in discordant breccia pipes [4]. In the OML, later secondary alteration processes (both hypogene and supergene) transformed parts of the original sulfide bodies into nonsulfide ores [7,8]. In the Tsumeb and Berg Aukas area, nonsulfide ores consist of various oxidized Zn-Pb-Cu-minerals, like carbonates, silicates, phosphates, vanadates and many others [2]. Germanium is also locally remobilized in both the hydrothermal or supergene oxidized minerals, like willemitite or Fe-oxy-hydroxides, and also forms proper secondary minerals (e.g., stottite [9,10]). In the northeast extension of the Namibian Damara Belt in northwest Botswana, to our knowledge, only few Zn-Pb > (Cu-Ag-V-Ge) mineralizations have been already identified. These are represented by the Kihabe and Nxuu prospects, both owned by Mount Burgess Mining N.L. These exploration projects are located in the Aha Hills (Ngamiland District), near the Dobe border gate with Namibia (Figures 2 and 3). The Kihabe prospect contains Zn-Pb resources (compliant to the 2004 Australasian Code for Reporting of Exploration Results, Mineral Resources and Ore Reserves – JORC code) of 14.4 million tons at 2.84% zinc equivalent, and an Ag amount of 3.3 million ounces. The Nxuu Zn-Pb resources are currently estimated at around 10.9 million tons at 3.20% zinc equivalent. Even though V and Ge have been detected in both prospects, these elements have not been included yet in the resource estimate [11]. The Kihabe and Nxuu mineralizations consist of mixed sulfide–nonsulfide bodies hosted in Neoproterozoic rocks. In this paper, we present the results of a mineralogical and geochemical study, conducted on drillcore samples of the Kihabe prospect, delineating a possible genesis of its sulfide–nonsulfide ores, in comparison with similar mineral deposits located in the region.

2. Geological Setting

2.1. Regional Geology

In the Ngamiland District, the Pan-African Damara Belt extends from Namibia in the SW, northwest Botswana to Zambia and Congo in the NE (Figure 1; [12]). As most of the Precambrian basement is covered by a blanket of Kalahari sedimentary rocks and various lithotypes belonging to the Karoo Supergroup, the reconstruction of its tectonic framework is partly unclear, and mostly based on the interpretation of geophysical data [12–18]. The study area is located northwest of the Ghanzi–Chobe zone, a NE-trending Meso- to Neoproterozoic belt, formed following the tectonic inversion of the Northwest Botswana rift, during the Damara Orogenesis (Figure 2; [12]). Within this domain, the younger rocks comprise clastic and carbonate lithotypes of the Ghanzi Group, which has been correlated with the Tsumis and Nosib groups in southwest Namibia [17,19–21].

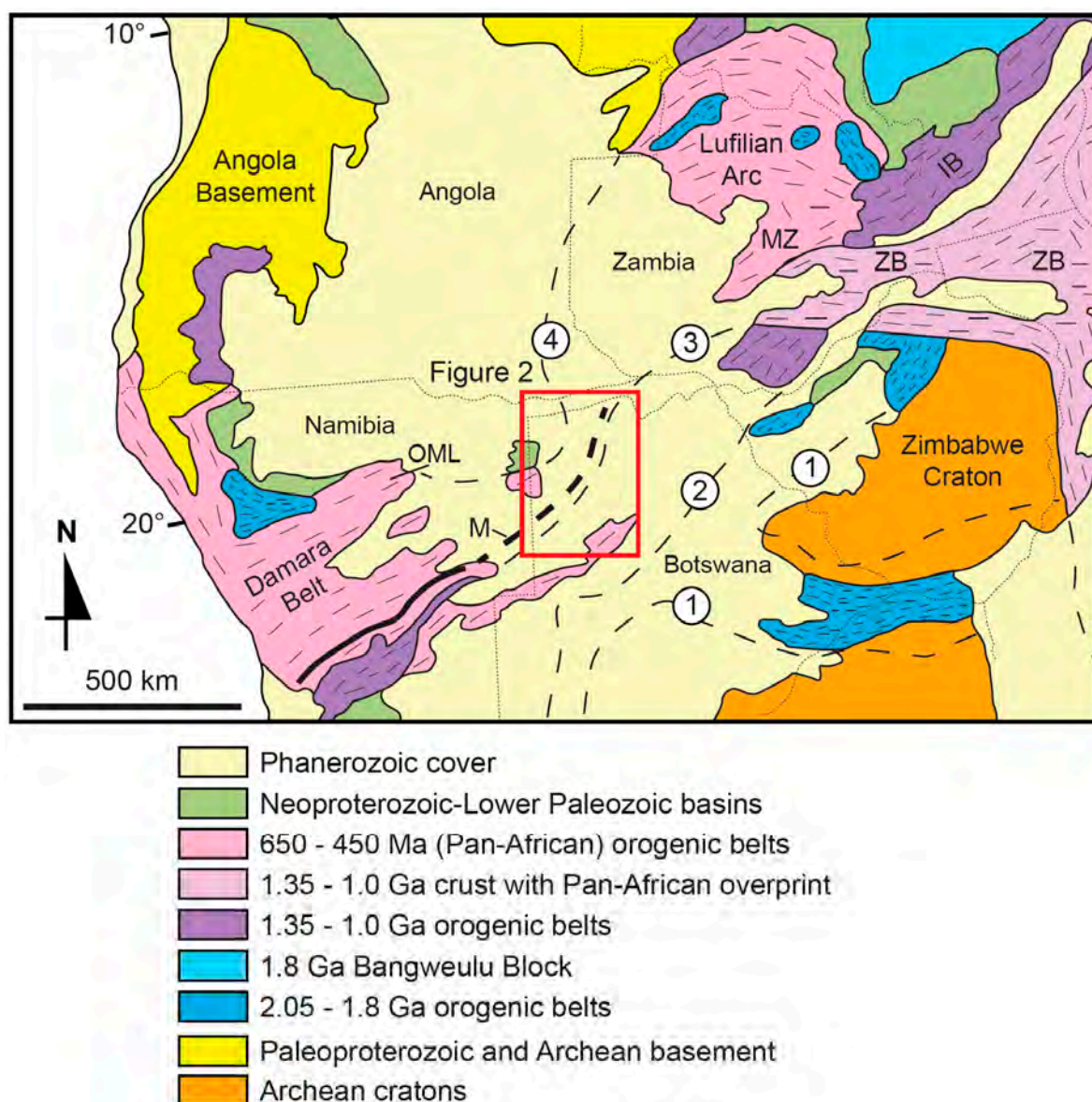


Figure 1. Precambrian tectonic framework of Southern Africa (modified from [22]). ① western edge of Archean cratons; ② boundary between 2.05–1.8 Ga orogenic belts and 1.35–1.0 Ga belts; ③ boundary between 1.35–1.0 Ga belts and Pan-African belts; ④ western edge of Pan-African belts. IB = Irumide Belt; M = Matchless Belt; OML = Otavi Mountainland; ZB = Zambezi Belt. The red square indicates the position of map in Figure 2.

Following Key and Ayers [13] and Singletary et al. [17], the basement occurring in the Ngamiland District, northwest of the Ghanzi–Chobe zone, consists of four units (Figure 2):

(1) the Kwando Complex, a geophysically distinct subsurface terrain, likely consisting of granite gneiss (of uncertain Precambrian age);

(2) a domain, which is considered to be the NE extension of the main part of the Damara Belt in Botswana [12], characterized by northeast-structural trending meta-sedimentary and meta-igneous rocks. This domain is composed of four juxtaposed terrains: (i) the Roibok Complex (amphibolite and mafic schists, correlated with the Neoproterozoic Matchless Belt of southern Damara Orogen [23]); (ii) the Koanaka Group (Neoproterozoic), consisting of strongly deformed, greenschist-facies meta-sedimentary rocks and marbles outcropping in the Kihabe and Koanaka Hills [12,13]; (iii) the Chihabadum Complex (Neoproterozoic?), made up of igneous and meta-igneous rocks; and (iv) the lower grade Aha Hills

Formation (Neoproterozoic; [13]), consisting dominantly of chert-rich marble and dolomite exposed in the Aha Hills, which could be correlated with the lithotypes of the Otavi Group in Namibia [12];

(3) the Quangwadum Complex (Paleoproterozoic), that is represented by a granitic-gneissic basement massif, outcropping on the northern slopes of the Aha Hills;

(4) the Xaudum and Tsodilo Hills groups, which comprise meta-sedimentary rocks characterized by strong north-to-northwest structural trends, occurring north of the Quangwadum Complex. The Xaudum Group is composed of folded, low metamorphic grade fine-grained marbles, carbonate rocks with chert, quartzites and slates. The Tsodilo Hills Group comprises kyanite-grade quartz–muscovite schists, meta-conglomerates, ferruginous quartzites and biotite-gneisses. The groups are considered to have either a Paleoproterozoic [13] or a Neoproterozoic age [17]. In greater detail, Singletary et al. [6] correlate the Xaudum Group with the Nosib Group, and the Tsodilo Hills Group with the glaciogenic rocks of the Chuos Formation of the Damara succession in Namibia.

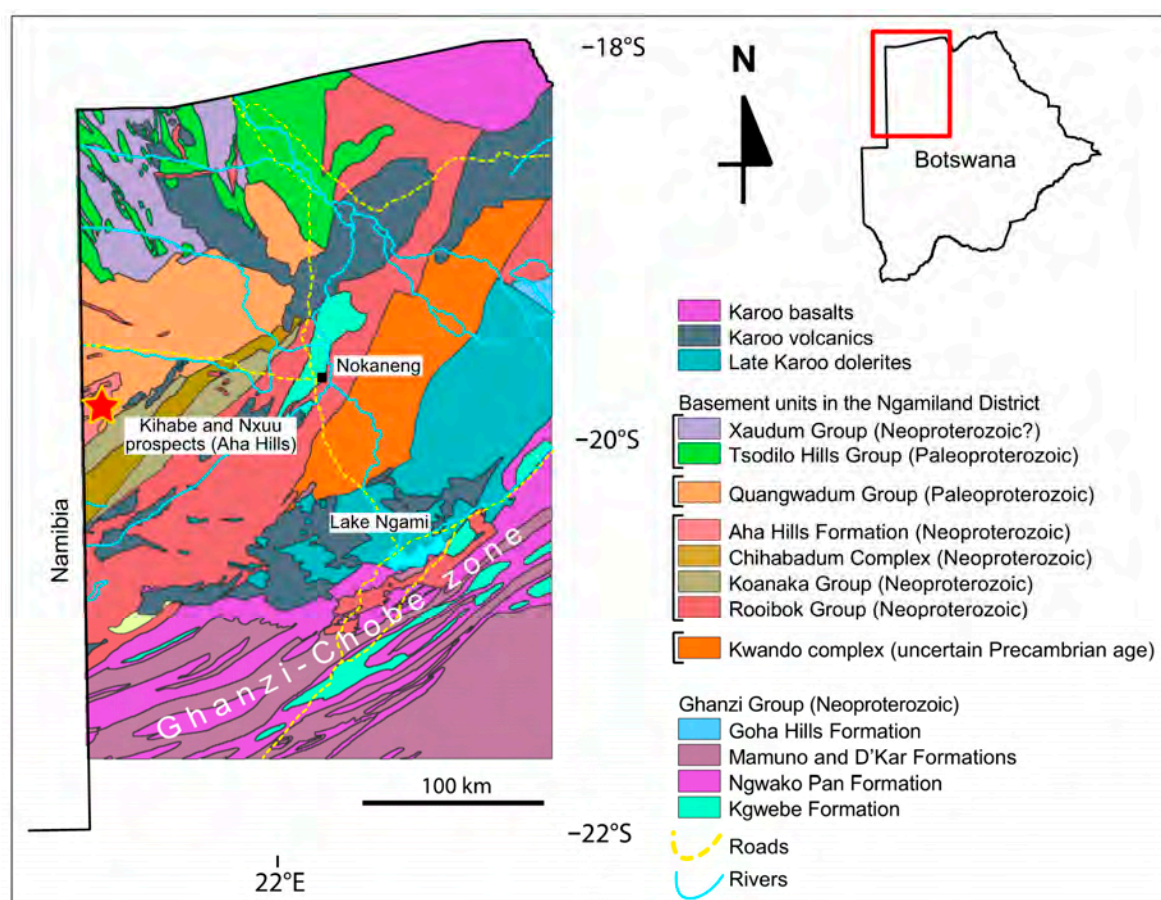


Figure 2. Subsurface geological map of northwestern Botswana, with the location of the Kihabe and Nxuu prospects (modified from [13]). The Kalahari cover is not shown.

According to other authors (e.g., [15] and references therein), the meta-sedimentary successions occurring in the Ngamiland District, both to the north and to the south of the granitic–gneissic Quangwadum Complex, have to be subdivided into only two units: the Xaudum Group and the Tsodilo Hills Group. The Xaudum Group is considered to be a part of the Ghanzi–Chobe Supergroup together with the Roibok Formation and the Ghanzi Group, and should have a Neoproterozoic age. The Tsodilo Hills Group has instead a Paleoproterozoic age (after zircon dating; [15]), and thus predates the Xaudum Group and the other meta-sedimentary rocks of the Damara sequence in northwest Botswana.

2.2. The Kihabe Prospect

Anomalous Zn-Pb values in the Aha Hills were detected at first during a regional geochemical survey, carried out by the Geological Survey of Botswana in the early 1980s [24]. These anomalous concentrations were later confirmed by Billiton explorative work (Grids 30-1 and 30-2; [25]), and delineated within flat valleys, characterized by a fairly thick drift cover. After having undertaken detailed geochemical surveys, the company drilling intersected some secondary pyromorphite and vanadinite mineralizations at depths ranging from 8 to 15 m within the Kalahari sedimentary rocks [26]. The anomalous Zn-Pb contents in the surficial sediments were revealed to be lying directly above the current known Kihabe mineralization.

The Kihabe prospect (Figure 3) has a strike length of 2.4 km, and could be mined with two open-cut pits covering a total length of 1.8 km. It is estimated that the two proposed pits will have strip ratios in the order of 4.5:1. Within the 1.8 km of strike, the average width of the deposit is 27 m, from 5 m below surface to 175 m depth. This depth corresponds to the maximum extent of the drillholes to date (2019; [11]). Many sections of the Kihabe resource are between 35 m and 60 m wide (Figure 4). The mineralization is covered by 5 to 15 m of Kalahari sedimentary rocks (Figure 4), and consists of stratabound orebodies hosted in a quartzwacke, at the contact with the barren dolostone, which have been deformed by folding and minor faulting (Figure 4). Following Key and Ayers [13], the host rock belongs to the Aha Hills Formation. The orebody is elongated along a general NE–SW direction and appears to be localized in steeply dipping isoclinal fold limbs (Figure 4; [27]). The sulfide mineralization at Kihabe, which represents 75% of all the ore, has been regarded as a sedimentary-hosted massive sulfide (SHMS) or Mississippi Valley type deposit [25,27]. Approximately 25% of the more surficial part of the orebody shows supergene alteration (Figure 4; [27]). Previous studies conducted in this zone revealed that Zn is mainly hosted in smithsonite and baileychlore. Lead is concentrated predominantly in galena remnants, as well as in minor Pb-oxidized minerals, whereas V is associated with descloizite [11]. Significant intersections of V have also been defined in zones outside the perimeter of the known Zn-Pb mineralization, leading to a possible expansion of the current resource area [11]. Metallurgical test work on the Kihabe sulfide ores has shown that good Zn and Pb recoveries are achieved through flotation. The Kihabe oxidized ore can instead be treated through solvent extraction and electrowinning methods (SX-EW) [11].

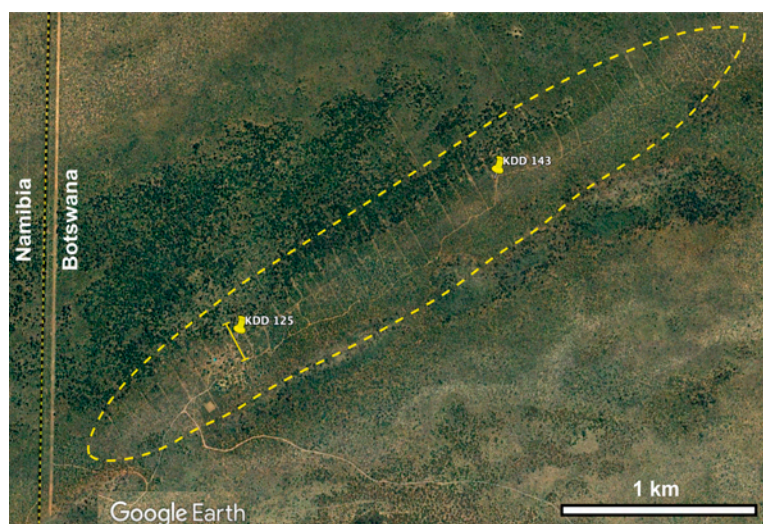


Figure 3. Satellite photograph of the Kihabe prospect (from Google Earth; image 2008), with the position of the analyzed drill holes: KDD 125: 19°42′3.81″ S latitude, 21°0′29.78″ E longitude; and KDD 143: 19°41′38.37″ S latitude, 21°1′15.71″ E longitude. The yellow dashed line represents the outline of the mineralization. In correspondence of the drill hole KDD 125, the projection of the geological section depicted in Figure 4 is indicated.

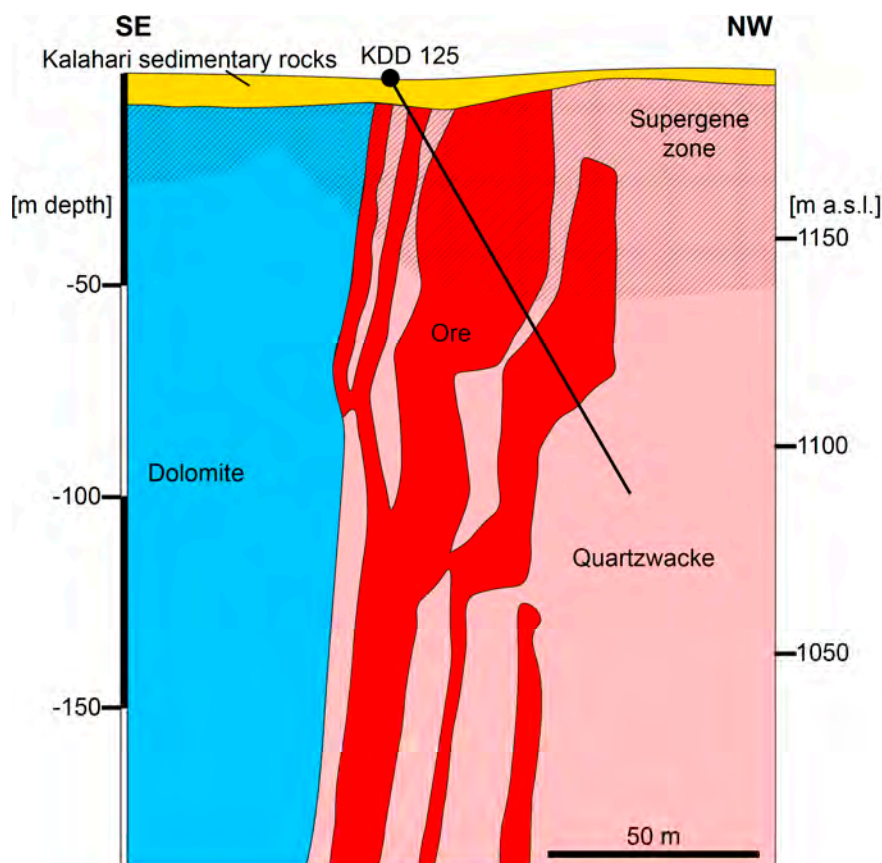


Figure 4. Schematic geological section of the Kihabe mineralized body (modified from [11]). Ore = outline of the ore bodies based on drillcore 3D modeling [11]. See Figure 3 for the location of the cross section within the prospect area.

3. Materials and Methods

For this study, we analyzed 30 samples (Table 1) collected by the Mount Burgess personnel, from two drillcores located in two distinct areas of the Kihabe project (Figures 3 and 5): KDD 125 from the southwestern zone ($19^{\circ}42'3.81''$ S latitude, $21^{\circ}0'29.78''$ E longitude; interval 55.00–60.90) and KDD 143 in the northeastern zone ($19^{\circ}41'38.37''$ S latitude, $21^{\circ}1'15.71''$ E longitude; interval 50.00–54.93).

Small slabs from the core samples have been cut, in order to get polished thin section preparations for petrographic and mineralogical analysis using conventional optical and scanning electron microscopy (SEM), equipped with energy dispersive spectroscopy (EDS). The remaining material was then crushed and homogenized for whole-rock chemical analysis and qualitative X-ray powder diffraction (XRPD).

Representative powder samples for each drillcore were obtained by first crushing the sample in a jaw crusher and then sieving to <2 mm. These fragments were then repeatedly split, using an Endecott stainless steel hand-held 50/50 sample divider (6.35 mm slot) until a ~ 20 -g representative sample was obtained. This was then milled with an agate pot and put in a Tema mill until a fine-grained powder material was obtained (30–90 s depending upon rock hardness). This powder was used for whole rock chemical analyses of major and minor elements. Whole rock chemical analyses were carried out at the Bureau Veritas Analytical Laboratories Ltd. (Vancouver, BC, Canada). The pulverized samples were subjected to LiBO_2 - LiB_4O_7 fusion (to measure SiO_2), and 4-acid digestion. The analyses were carried out by ICP-ES (multi-element inductively coupled plasma emission spectrometry)-ICP-MS (multi-element inductively coupled plasma mass spectrometry) for 41 elements. Concentrations above detection limits were obtained for 35 elements.

Table 1. List of studied drillcore samples, with mineralogy inferred by qualitative XRPD.

Drillcore	Sampled Interval	Sample Label	Mineral Assemblage
KDD125	55.00–55.34	KDD 125-1	Qz, Ms, Cer
	55.34–55.76	KDD 125-2	Qz, Ms, Ang
	55.76–56.05	KDD 125-3	Qz, Ms, Ang, Sp, Hem
	56.05–56.50	KDD 125-4	Qz, Ms, Sp, Gn, Py
	56.60–57.00	KDD 125-5	Qz, Ms, Sp, Gn, Py, Hem
	57.00–57.30	KDD 125-6	Qz, Ms, Sp, Gn, Sm, Py, Hem
	57.30–58.07	KDD 125-7	Qz, Ms, Or, Cer, Gn, Sm
	57.08–58.57	KDD 125-8	Qz, Ms, Sm, Sp, Gn, Hem
	58.57–58.89	KDD 125-9	Qz, Ms, Sp, Gn, Hem
	58.89–59.10	KDD 125-10	Qz, Ms, Sp, Gn, Py
	59.10–59.96	KDD 125-11	Qz, Ms, Sp, Gn, Py, Hem
	59.96–60.10	KDD 125-12	Qz, Ms, Hem
	60.10–60.32	KDD 125-13	Qz, Ms, Sp, Gn, Sm, Hem
	60.32–60.63	KDD 125-14	Qz, Ms, Or, Kln, Gn, Cer
	60.63–60.90	KDD 125-15	Qz, Ms, Or, Gn, Cer
KDD143	50.00–50.04	KDD 143-16	Qz, Ms, Sm, Wlm
	50.04–50.40	KDD 143-17	Qz, Ms, Sm, Wlm, Hem
	50.40–50.72	KDD 143-18	Qz, Ms, Or, Sm, Blc, Cer
	50.72–50.92	KDD 143-19	Qz, Ms, Or, Sm, Blc
	50.92–51.24	KDD 143-20	Qz, Ms, Or, Sm, Blc, Hem
	51.24–51.60	KDD 143-21	Qz, Sm, Ms, Blc, Ill, Or
	51.60–51.86	KDD 143-22	Qz, Ms, Or, Sm, Blc, Ill
	51.86–52.20	KDD 143-23	Qz, Sm, Ms, Or, Blc, Wlm, Mim, Cer
	52.20–52.55	KDD 143-24	Qz, Sm, Ms, Blc, Mim, Cer, Or
	52.55–52.72	KDD 143-25	Qz, Blc, Or, Ms, Cer, Sau, Ill
	52.72–53.00	KDD 143-26	Qz, Blc, Or, Ms, Cer, Sau, Ill, Wil, Sm
	53.00–53.93	KDD 143-27	Qz, Ms, Or, Blc, Cer
	53.93–54.26	KDD 143-28	Qz, Ms, Blc, Sm
	54.26–54.65	KDD 143-29	Qz, Ms, Cer, Gn, Sm
	54.65–54.93	KDD 143-30	Qz, Ms, Cer, Gn, Sm, Wlm

Minerals are listed in order of abundance, qualitatively evaluated on the basis of bulk rock chemical compositions. Ang = Anglesite; Blc = baileychlorite; Cer = cerussite; Gn = galena; Hem = hematite; Ill = illite/smectite (inferred with the support of SEM-EDS; see text for details); Kln = kaolinite; Mim = mimetite; Ms = muscovite; Or = orthoclase; Py = pyrite; Qz = quartz; Sau = sauconite; Sm = smithsonite; Sp = sphalerite; Wlm = willemite.



Figure 5. Pictures of drillcore trays with the analyzed drillcore intervals (enclosed in the red line): KDD 125: interval 55.00–60.90; and KDD 143: interval 50.00–54.93. In both the cores it is possible to see reddish intervals, affected by supergene alteration.

X-ray powder diffraction (XRPD) analysis for mineral phase identification was carried out on identical powder splits to those used for whole rock chemical analyses. X-ray powder diffraction analysis was carried out at the Institute of Earth Sciences, Heidelberg University (Germany), with a Siemens D 500 Bragg-Brentano X-ray diffractometer, with $\text{CuK}\alpha$ radiation, 40 kV and 30 mA, 5 s/step and a step scan of $0.05^\circ 2\theta$. The data were collected from 3 to $110^\circ 2\theta$. Relative abundances between the minerals were qualitatively determined on the basis of the bulk rock chemical analyses of the samples, and the chemical compositions of identified minerals.

The thin sections were firstly examined under a petrographic microscope with both transmitted and reflected light. Scanning electron microscopy observations and back-scattered electrons (BSE) imaging were carried out on selected polished thin sections from material with the highest metallic grades. The carbon-coated sections were analyzed with a JEOL JSM5310 instrument at the University of Napoli. Element mapping and qualitative EDS spectra were obtained by the INCA microanalysis system equipped with an Oxford energy dispersive spectrometry INCA X-stream pulse processor and the 4.08 version Inca software. The operating conditions were an acceleration voltage of 15 kV, 50–100- μA filament current, variable spot size and a working distance of 20 mm. The reference standards used for quantitative microanalysis were anorthoclase, Si, Al and Na; diopside, Ca; microcline, K; rutile, Ti; fayalite, Fe; olivine, Mg; serandite, Mn; sphalerite, Zn; benitoite, Ba; celestite, Sr; fluorite, F; halite, Cl; pyrite, S; galena, Pb; and pure metal, Cu. Detection limits of the analyzed elements are below 0.1%.

4. Results

Sulfides were detected preferentially in the drillcore KDD 125, whereas oxidized minerals occur in both analyzed cores. Willemite and baileychlore were detected only in core KDD 143 (Figure 6; Table 1; Table 2). The meta-quartzwacke host rock is characterized by abundant fine-grained quartz and minor feldspar clasts (Table 1), with an intergranular matrix made up of micas and other phyllosilicates, some occurring as distinctly schistose muscovite aggregates, and some others showing a finer decussate structure (Figure 7a–d). Micas have a muscovite composition, with minor amounts of Mg (ca. 1 wt. % MgO). Fine newly-formed silica (silicification) has also been observed. The quartzwacke contains several types of detrital minerals in traces, like ilmenite, rutile, monazite, tourmaline and zircon.

Table 2. Summary of the ore minerals detected in the Kihabe samples, with their International Mineralogical Association (IMA)-accepted chemical formulas.

Mineral	Formula
Anglesite	PbSO_4
Argentite	Ag_2S
Baileychlore	$(\text{Zn,Fe}^{2+},\text{Al,Mg})_6(\text{Si,Al})_4\text{O}_{10}(\text{OH})_8$
Cerussite	PbCO_3
Galena	PbS
Hemimorphite	$\text{Zn}_4(\text{Si}_2\text{O}_7)(\text{OH})_2\cdot\text{H}_2\text{O}$
Hinsdalite	$\text{PbAl}_3(\text{SO}_4)(\text{PO}_4)(\text{OH})_6$
Iodargyrite	AgI
Mimetite	$\text{Pb}_5(\text{AsO}_4)_3\text{Cl}$
Pyromorphite	$\text{Pb}_5(\text{PO}_4)_3\text{Cl}$
Sauconite	$\text{Na}_{0.3}\text{Zn}_3(\text{Si,Al})_4\text{O}_{10}(\text{OH})_2\cdot 4\text{H}_2\text{O}$
Smithsonite	ZnCO_3
Sphalerite	ZnS
Willemite	Zn_2SiO_4

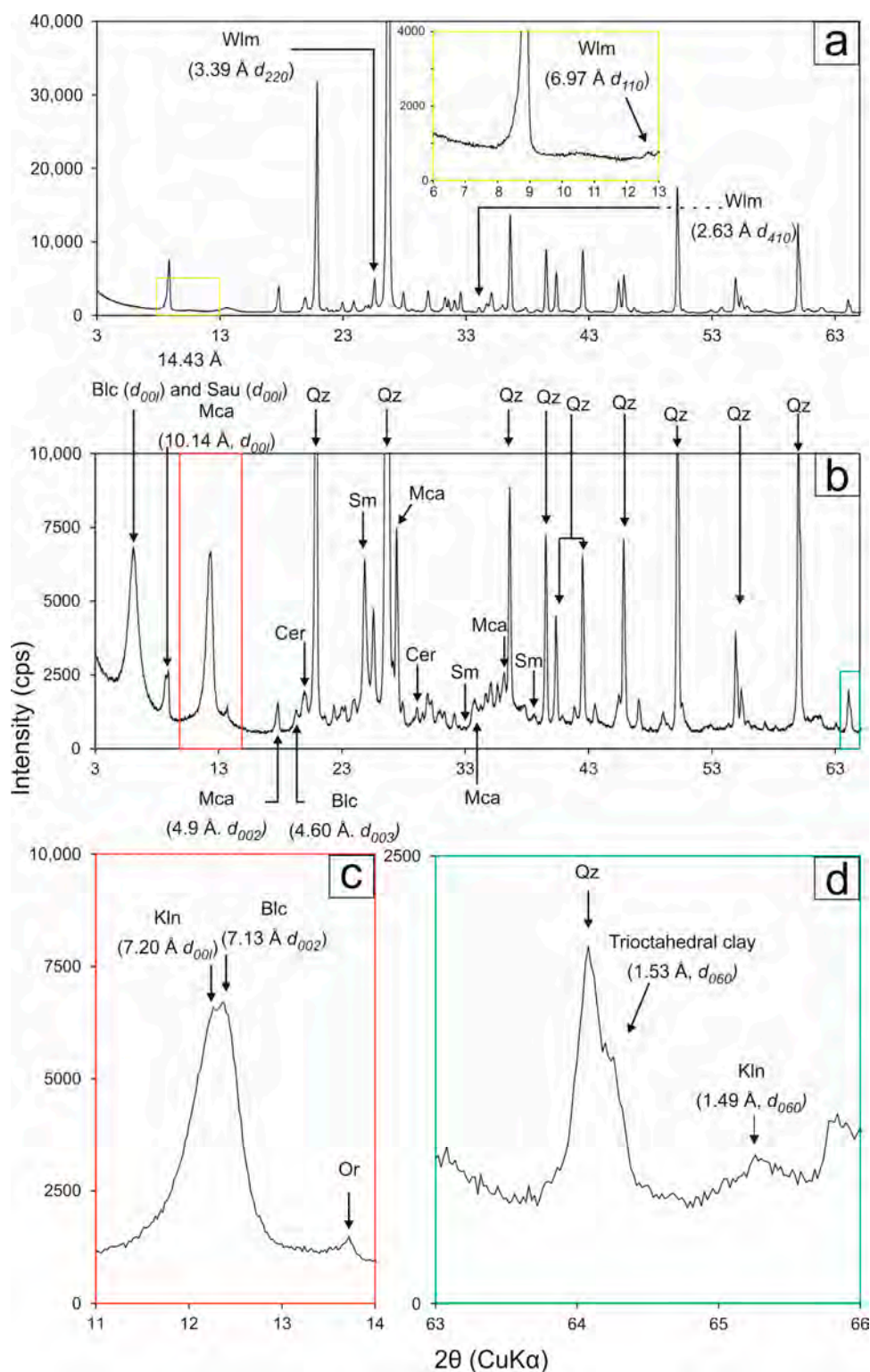


Figure 6. Examples of XRPD patterns of willemite- and baileychlore-bearing samples: (a) Sample KDD143-16: XRPD pattern showing characteristic peaks of willemite (other minerals identifiable in the pattern are quartz, muscovite and smithsonite; see Table 1); (b) Sample KDD143-26: XRPD pattern showing characteristic peaks of major phases occurring in the sample; (c) and (d) enlargements of (b) showing characteristic peaks of baileychlore. Notes: unspiked peaks in the XRPD pattern of sample KDD143-26 correspond to minor reflections of orthoclase. Blc = baileychlore; Cer = cerussite; Kln = kaolinite; Mca = mica (undistinguished; see text for details); Or = orthoclase; Qz = quartz; Sau = sauconite; Wlm = willemite.

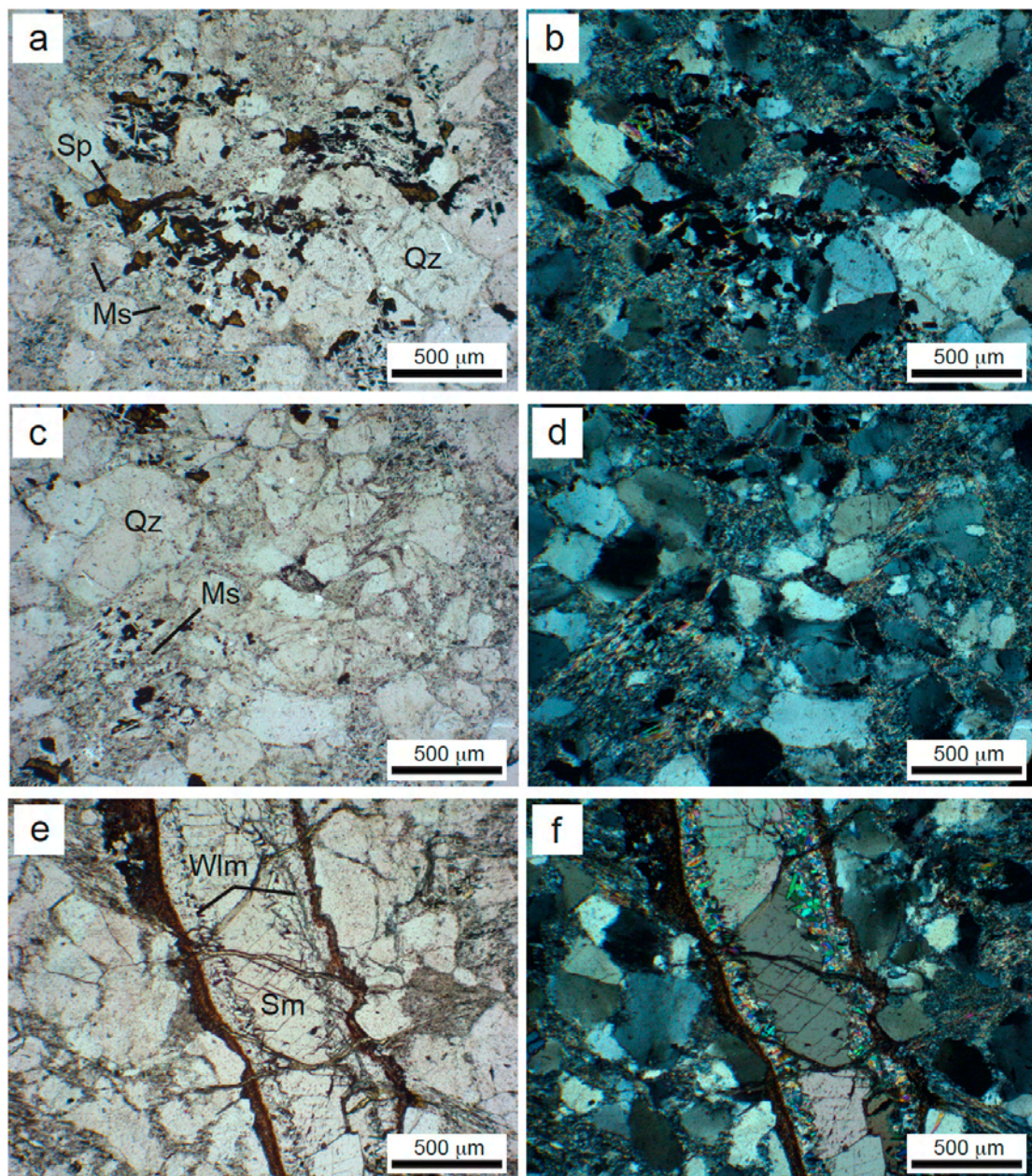


Figure 7. Transmitted light micrographs: (a) and (b) Sample KDD 125-8: Sphalerite dispersed in the quartzwacke matrix, in between micas with decussate structure (NII and N+); (c) and (d) Sample KDD 125-8: Quartzwacke with schistose structure (NII and N+); (e) and (f) Sample KDD 143-16: Vein consisting of willemite and smithsonite (NII and N+). Ms = muscovite; Qz = quartz; Sm = smithsonite; Sp = sphalerite; Wlm = willemite.

In the drillcore KDD 125, sphalerite appears to be interstitial in the quartzwacke (Figure 7a,b), intergrown with quartz and mica (Figure 8a). Locally, sphalerite is slightly ferroan (3–4 wt. % Fe) and can contain up to 1–2 wt. % Pb, with subordinate As (0.3 wt. %). Galena occurs either at the rim of the sphalerite crystals or in the porosity of the host rock (Figure 8a,b). Pyrite is relatively rare (Figure 8c), and contains variable amounts of As and Cu (rarely Co). Locally, arsenopyrite has been observed in association with sphalerite (Figure 8d). Argentite micrograins are dispersed within the above-mentioned mineral assemblage, both in the sulfides and the quartz gangue. At the microscale, sulfides appear clearly deformed, following the foliation pattern of the quartzwacke host

rock (Figure 8b). In the drillcore KDD 143, sulfides are rather rare, and only occur as local relicts within quartz cements. Barite occurs as a rare accessory phase.

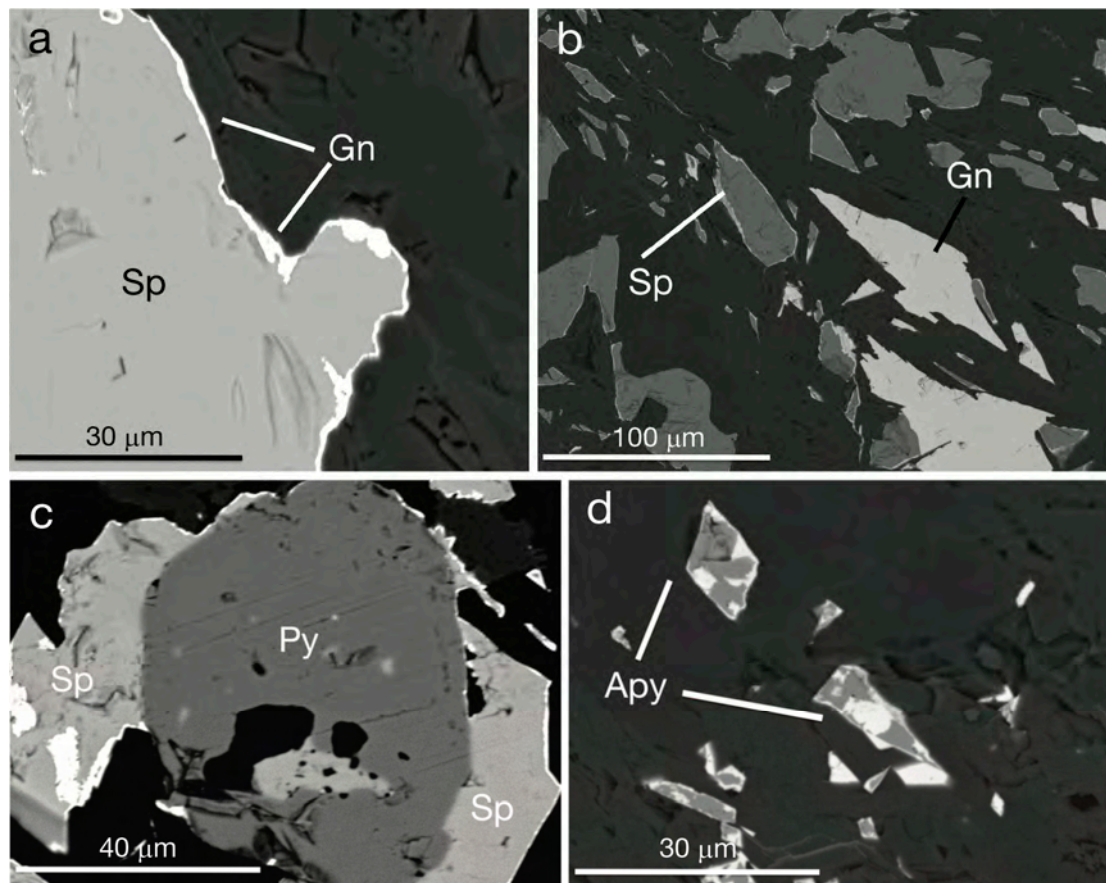


Figure 8. Backscatter electron SEM micrographs of sample KDD 125-8. Mineral chemistry was determined through EDS. (a) Sphalerite with galena border associated with quartz grains; (b) Sphalerite and galena elongated within the quartzwacke; (c) Pyrite grain associated with sphalerite; (d) Arsenopyrite intergrown with As-rich sphalerite. Apy = arsenopyrite; Gn = galena; Py = pyrite; Sp = sphalerite.

Willemite has been detected via the XRPD and by observation of thin sections (Table 1; Figures 6a and 7e,f). It occurs as patches and/or vein filling (Figure 7e,f and Figure 9a–d), forming two generations: the first one generally forms small allotriomorphic masses, as a cement of the host rock (Figure 9a) and appears slightly deformed, whereas the second generation forms euhedral micro- to macro-crystals in veins and cavities, and does not show peculiar deformation structures (Figure 9b,c). Both willemite generations can be As-rich (up to 2.5 wt. % As_2O_5 ; Table A1).

Among the sampled cores, baileychlorite is only present in the willemite-bearing samples (Table 1). The Zn-chlorite was identified with the XRPD method, through the characteristic d_{hkl} peaks at 14.290 Å (d_{001}), 7.145 Å (d_{002}) and 1.53 Å (d_{060}) (Figure 6b–d; [28]). This Zn-bearing chlorite texturally grows in the porosity of the country rock, upon and between preexisting mica packages, and it appears to locally replace K-feldspar (Figure 10a–e). In some cases, when baileychlorite substitutes K-feldspar, it is texturally associated with kaolinite and galena (Figure 10b,c).

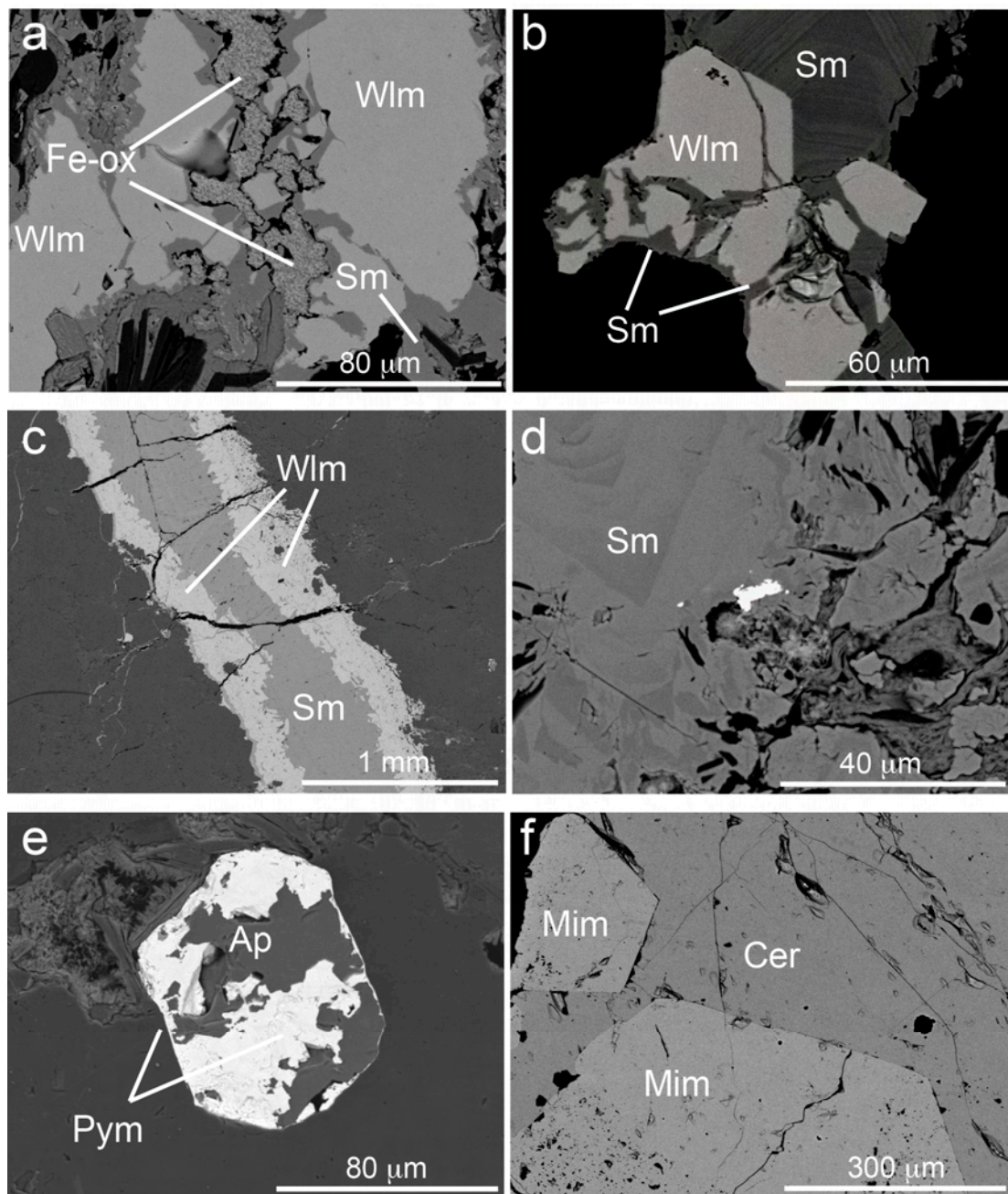


Figure 9. Backscatter electron SEM micrographs. Mineral chemistry was determined through EDS. (a) KDD 143-22. Willemite altered and partially replaced by smithsonite and Fe-oxy-hydroxides; (b) KDD 143-23. Idiomorphic willemite crystals, vein-crossed and partially altered to zoned smithsonite; (c) KDD 143-16. Thin willemite vein, internally filled with smithsonite; (d) KDD 143-16. Zoned crystals of smithsonite; in the center small galena remnant; (e) KDD 143-26. Fluorapatite crystal patchily replaced (Pb → Ca and Cl → F) by pyromorphite; (f) KDD 143-23. Idiomorphic mimetite crystals embedded in cerussite. Ap = fluorapatite; Cer = cerussite; Fe-ox = Fe-oxy-hydroxides; Mim = mimetite; Sm = smithsonite; Wlm = willemite.

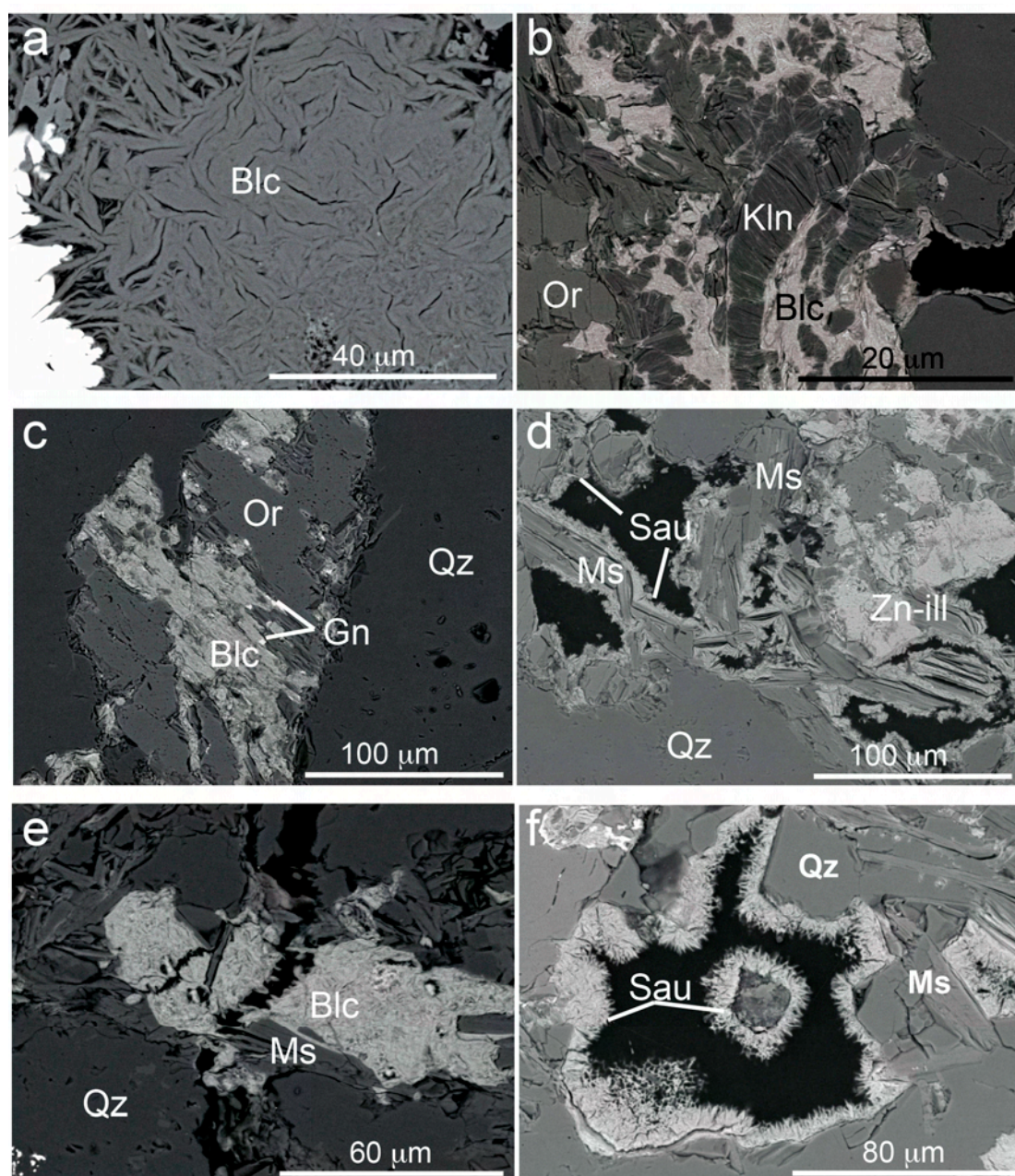


Figure 10. Backscatter electron SEM micrographs. Mineral chemistry was determined through EDS. (a) KDD 143-23. Baileychlore packages, randomly oriented, filling porosity; (b) KDD 143-22. Baileychlore associated with kaolinite replacing orthoclase; (c) KDD 143-26. Orthoclase crystal from the host quartzwacke partially replaced by baileychlore; fine galena is associated with the Zn-chlorite; (d) KDD 143-26. Sauconite and Zn-bearing illite growing in dissolution cavities, above mica packages; (e) KDD 143-22. Patches of baileychlore growing in between mica packages and quartz grains; (f) KDD 143-26. Dissolution cavity bordered by freely growing sauconite. Blc = baileychlore; Gn = galena; Kln = kaolinite; Ms = muscovite; Or = orthoclase; Qz = quartz; Sau = sauconite; Sm = smithsonite; Zn-ill = Zn-bearing illite.

Differently from the compositional data quoted in the literature (Table A2; [28]), the zinc content of the Kihabe baileychlore is higher, ranging from 37.5 to 47.6 wt. % ZnO, and is associated with MgO values varying between 1.5 and 3.5 wt. %, slightly lower Al₂O₃ contents between 10 and 16 wt. %, and SiO₂ between 26 and 31 wt. %. The Kihabe baileychlore has relatively low FeO_t contents (< 1 wt. %) (Table A2). In a few analyses, Cu concentrations of ca. 1 wt. % have been detected. Although

SEM-EDS is not the best method for measuring the chemical composition of phyllosilicates, based on the mentioned chemical composition, baileychlore structure formulae calculated for 28 oxygen equivalents do not give results very different from the IMA-accepted formula (Table A2; [28]). Si has an average value of 3.47 apfu, and Al^{VI} is on average 1.30 apfu, whereas Mg ranges between 0.28 to 0.63 apfu, and Zn between 3.20 and 4.28 apfu. Iron, evaluated as Fe²⁺, has a maximum occupancy of 0.17 apfu. Among these data, the calculated Si apfu show no variation respect to Zn apfu, whereas there are clear inverse correlations between Si and R²⁺ (Zn, Fe, Mg) apfu and Al^{VI} apfu (Table A2). Among the other phyllosilicates, sauconite occurs as a late-stage phase growing in cavities, and is commonly associated with Zn-bearing illite. The last one probably consists of illite/smectite (sauconite) mixed layers (e.g., sample KDD 143–26; Figures 6b and 10e,f).

Smithsonite occurs in two generations in both the analyzed cores. In the first generation, it appears as a local replacement of sphalerite or willemite, and shows minor As amounts retained from the altered Zn-silicate (Figure 9a,b). A second smithsonite phase forms concretions in cavities and fills pore spaces in the host rock (Figure 9c,d). This concretionary smithsonite is commonly chemically zoned (Figure 9d), with alternating bands containing variable Mg amounts (up to 4 wt. % MgO, Table A1).

Cerussite is the most common oxidized Pb-mineral at Kihabe in both the analyzed cores (Table 1), though it occurs in small patches and locally, as euhedral crystals in association with Fe-oxy-hydroxides. It may contain small amounts of Zn. Anglesite was detected in traces only by XRD (Table 1). Pyromorphite occurs as cement in the country rock or as replacements along the rims of fluorapatite (Figure 9e; Table A3). Mimetite locally occurs as euhedral crystals intergrown with cerussite (Figure 9f), and contains small amounts of phosphorus (Table A3). Hinsdalite was also detected in a couple of samples (KDD 125-5 and KDD 143-26). Silver is present as argentite inclusions in silica, but also in iodargyrite (Ag-iodide). Iron- and Mn-oxy-hydroxides, containing small amounts of Zn, Pb and Si, are widespread in both the cores (Tables 1 and A3).

Even though descloizite is reported by Mt Burgess Ltd. [11], as an abundant mineral in the most surficial section of the ore, this vanadate was not detected neither through XRPD nor at SEM-EDS in the samples analyzed for this study.

The results of the chemical analyses of 20 selected Kihabe samples are displayed in Table A4. Zinc shows values varying from <0.1% to 9% throughout the analyzed samples, with the highest concentrations in the KDD 143 drillcore. Lead is less enriched, with values ranging between 0.20% and 4.80%. Silver (8–113 mg/kg) is not strictly correlated with Pb, but is quite scattered in the samples with relatively high Pb values. Cadmium correlates with zinc, both in primary sulfides and in nonsulfides. Copper does not show high concentrations (4 to 1831 mg/kg), but its values are more abundant in the KDD 143 samples. Cobalt is relatively low, with the higher values (up to 32 mg/kg) found again in KDD 143. The As values range between 40 and 3.6 mg/kg. Vanadium reaches 260 mg/kg only in one of the examined samples, possibly indicating the presence of descloizite.

5. Discussion

The results of this study on the Kihabe prospect shed new light on the mineralizing processes, which occurred in northwestern Botswana, and on their correlation with ore deposit formation in the Namibian Damara Belt. Firstly, the Kihabe prospect hosts significant sulfide mineralization, mainly consisting of Fe-sphalerite and galena, finely disseminated in stratabound horizons within the meta-quartzwacke. The mineralization shows distinct deformation features both at the macroscale [27] and microscale, thus suggesting that sulfide emplacement occurred before or contemporaneously with the Damara Orogeny in the whole region (540–520 Ma, Figure 11; [29]). Considering that the sulfides host rock (the Aha Hills Formation) has been correlated with the Otavi Group in Namibia [17], it is possible to compare the Kihabe prospect with the ore deposits of the OML. Specifically, the orebodies in the Kihabe prospect have features in common with the Berg Aukas-type base metal deposits [4,5]. These common features are as follows: the predominance of Zn on Cu, the stratabound style structure, the limited control of faults on the sulfide mineralization, and the presence of a distinct Pan-African

deformation on the sulfide assemblage [4,5]. At the same time, the most remarkable difference of the Namibian ores is found in the distinct nature of the host rock, which at Kihabe is represented by meta-quartzwacke, whereas in the Namibian ores it is dolostone. The dolostone intersected by several drillcores in the Kihabe area is barren.

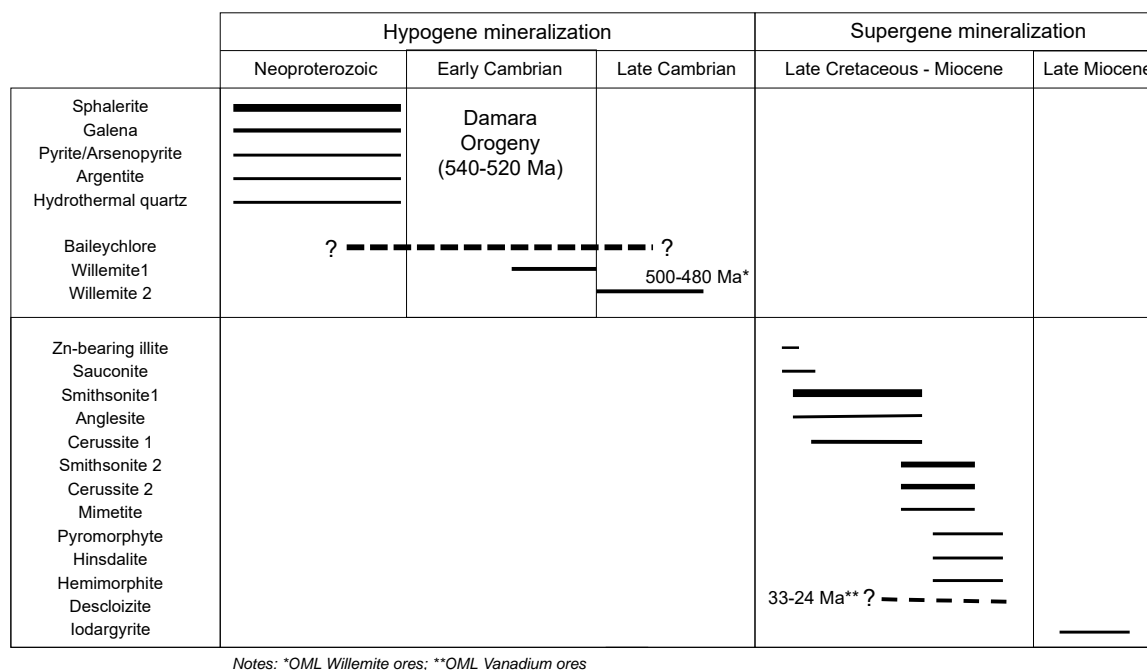


Figure 11. Mineral paragenesis of the Zn-Pb mineralization in the Kihabe area. Absolute ages after * [30], and ** [31].

In the nonsulfides assemblage, it appears that two types of mineralization styles occur in the investigated prospect: one characterized by minerals more typically found in hydrothermal ores (i.e., willemite and baileychlore; [7]), and a second one consisting of phases genetically related to real supergene processes (i.e., smithsonite, cerussite, Zn-Pb-phosphates, etc.; [7]). In detail, the presence of willemite at Kihabe is quite surprisingly, considering that the oxidized facies of the Kihabe mineralization was considered to be related to supergene alteration processes only. Specifically, two willemite types were identified: a first, deformed massive willemite generation, and a second generation consisting of euhedral hexagonal prismatic crystals. Compared to other willemite deposits [7,30,32], the Kihabe willemite should postdate sulfides emplacement, or even form at their expenses. However, we found no clear evidence of the latter process in the analyzed Kihabe samples, as is the case with the OML deposits [30]. Accordingly, this Zn-silicate could have originated either from the interaction of late-oxidizing hydrothermal fluids with preexisting sulfide bodies, or from the direct precipitation from Zn-bearing oxidizing fluids, focused along tectonic lineaments in formerly mineralized areas. The Kihabe willemite assemblage has many similarities with the willemite occurrences described in the Berg Aukas deposit [30]. In fact, the various willemite generations recorded at Berg Aukas have been comprehensively classified as (i) early willemites, occurring as fine-crystalline to granular masses replacing sphalerite, and (ii) later willemites, taking the form of semi-massive microcrystalline masses of hexagonal crystals. Absolute dating of the second willemite generation at Berg Aukas, carried out with the Rb-Sr geochronological method [30], produced ages which yield 499 ± 63 Ma and 493 ± 2 Ma, suggesting that its formation in the Otavi Mountainland was related to hydrothermal circulation during the waning stages of the Damara Orogeny, similarly to other structurally-controlled willemite mineralizations in Southern Africa (e.g., the Kabwe deposit [33,34]). Looking at the various mineralizing events that occurred in the Otavi Mountainland, it is likely that the Kihabe willemites formed in the same period (Figure 11), during the final stages of the Damara Orogeny [30]. However,

the high As concentration in the Kihabe willemite seems to be a peculiarity of this mineralized prospect, since this element rarely reaches maximum amounts of 1 wt. % in willemite, in particular structurally-controlled deposits, like Star Zinc, in Zambia [10]. The presence of As in the Kihabe willemite could be a result of the alteration of As-bearing sulfides (i.e., arsenopyrite), or could even indicate that the investigated Zn-silicate had a relatively high precipitation temperature (between 150 and 250 °C; [10]).

Baileychlore is common in the Kihabe KDD 143 core, particularly in those intervals containing willemite, whereas it is absent in the sulfide-bearing samples of the KDD 125 core. This Zn-bearing chlorite was identified for the first time by Rule and Radke [28] in the Red Dome deposit (North Queensland, Australia), a base- and precious-metal mineralization associated with calcsilicate skarn. In the above deposit [28], baileychlore occurs as a replacement of andesite and garnet-vesuvianite skarn clasts, occurring in a marble breccia. Although baileychlore was compared with other “similar” 14 Å-Zn-phyllsilicates identified in the high-T metamorphic Franklin deposit (New Jersey, UJ, USA), a supergene origin was postulated for the Red Dome Zn-chlorite [28]. Another more relevant baileychlore occurrence has been recently identified in the Prairie Downs volcanic-hosted massive sulfide (VHMS)-to SHMS-type Zn-Pb-(Cu-Ag) deposit, located in northwest western Australia [35]. In this deposit, baileychlore can be found in a broad alteration halo, extending also for more than 100 m in metabasalts surrounding the massive sulfide bodies [35]. Apparently, in the Prairie Downs deposit, baileychlore is not localized within the sulfide ore zone, but only at the border between the mineralization and the host rock, as well as in the barren zone around the orebody [35]. As in the case of VHMS deposits [36,37], this distribution was interpreted to be derived from the progressive migration of hydrothermal fluids through the porosity of the host rocks, laterally from the main feeder of the mineralization [35]. Specifically, in the Prairie Downs deposit, the Zn-chlorite was considered to have formed together with muscovite, as an alteration product of a clinozoisite–quartz protolith, developed from ZnCl₂- and KCl-rich hydrothermal fluids genetically related to sulfide mineralization [35]. The Kihabe mineralization seems to share a few similarities with the Prairie Downs deposit, in particular: (1) the spatial distribution of the baileychlore outside the sulfide ore zone, and (2) its scattered distribution throughout the host rock. It is more difficult, however, to find other analogies with Prairie Downs at the level of the deposit-type or the regional processes.

Going in detail into the microscopic structure of Kihabe baileychlore, this Zn-bearing chlorite appears to have mostly grown within the porosity, on top and in between preexisting mica packages. Baileychlore seems to replace the preexisting K-feldspars in the analyzed samples only to a limited extent. In some cases, where baileychlore substitutes for K-feldspar, it can be associated with kaolinite and galena. The porosity-filling and overgrowth textures can be considered as related to the direct precipitation of chlorite from solutions, where the preexisting 10 Å-phyllsilicates only acted as templates for the epitaxial or random crystallization of 14 Å-phyllsilicate on cleavage surfaces [38,39]. On the contrary, the substitution of feldspars might indicate a dissolution–crystallization mechanism, which could have been mediated by kaolinite. The latter mineral could represent either an intermediate phase of the replacement process, or a co-product derived from feldspar alteration. As it appears that the chlorite occurring in low-temperature systems derives from specific clay precursors through solid-state transformation mechanisms [38], whereas both direct precipitation and dissolution–crystallization processes are typical of hydrothermal systems [40], the textures described in the analyzed samples strongly suggest that Kihabe baileychlore is associated with the same hydrothermal processes that were responsible for the mineralization. To our knowledge, a specific geothermometer for baileychlore does not exist. However, by using the graphical semiempirical chlorite geothermometer of Bourdelle and Cathelineau [41], based on the Si and R²⁺ occupancy (in this case, we used the analyses obtained with SED-EDS; see values in Table A2), we estimated temperatures between 50 and 150 °C (Figure 12).

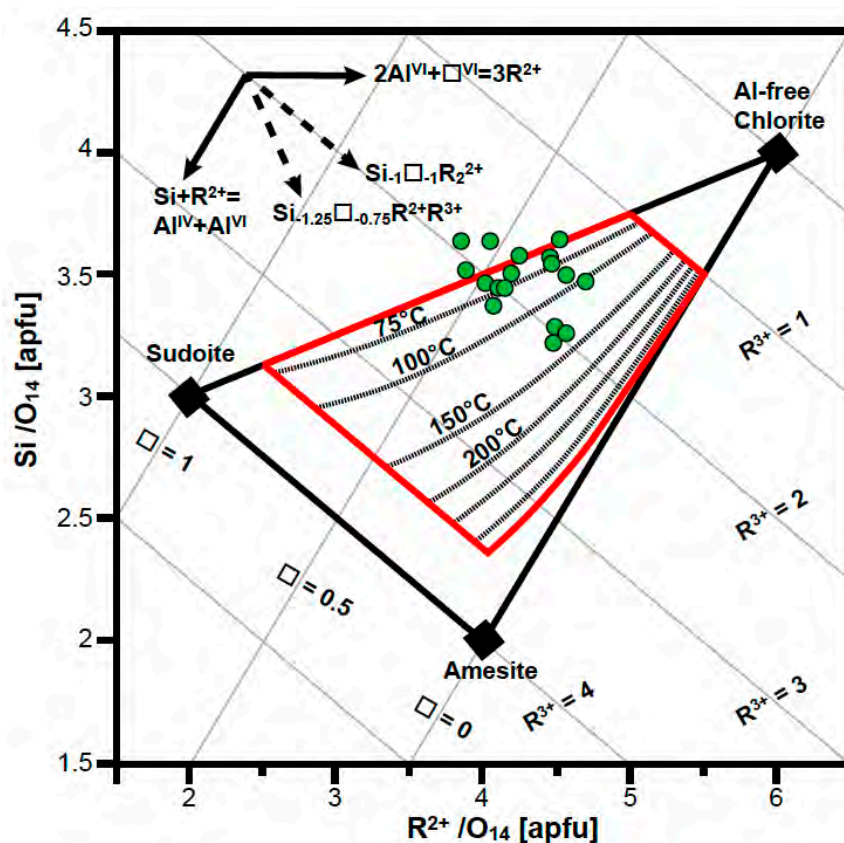


Figure 12. Semi-empirical graphical chlorite geothermometer of Bourdelle and Cathelineau [41], applied on the baileychlorite analyses obtained with this study. In the top-left corner, the element substitution vectors are shown.

Although the above data must be considered with the utmost care, because the geothermometer is not calibrated on baileychlorite and the analyses were carried out with the EDS method, at a rough scale the values are in agreement with the theoretical hydrothermal genesis of the Kihabe Zn-chlorite. This would also be coherent with the paragenetic association of baileychlorite with willemite. This considered, the peculiar association of baileychlorite with galena (and kaolinite), observed where the Zn-chlorite replaces feldspar, could be related to the cooling and neutralization of the acidic species ZnCl^+ and PbCl^+ during the infiltration of the hydrothermal fluid into the country rock, following a process well-described for the propylitic alteration bands around porphyry Cu systems [42], which produces assemblages of chlorite and sulfides in traces similar to those detected at Kihabe. This textural characteristic, in conjunction with the broad similarity between the occurrence of Zn-chlorite at Kihabe and the hydrothermal halo of the Prairie Downs deposit [35], raises further questions on the origin of the Kihabe baileychlorite. Specifically, it remains still unclear if the Kihabe Zn-chlorite represents a hydrothermal alteration associated with the primary sulfide mineralization, or if it is instead genetically related to the willemite precipitation (Figure 11). In any case, it seems unlikely that baileychlorite has a supergene origin, and that it is only localized in the more surficial supergene alteration zone [11], although further analyses are required to shed more light on the last point.

In the analyzed samples, sauconite was detected only in a few samples with XRD and SEM-EDS (Table 1). Here, it occurs as a late-stage phase growing in cavities, as a replacement of baileychlorite, or included in illite–smectite mixed layers. Similar textures have been observed in the Skorpion (Namibia; [43]) and Yanque (Peru; [44]) deposits. In both cases, sauconite in cavities and overlying muscovite/illite was considered to derive from neomineralization processes. In the Skorpion deposit, the formation of sauconite at the expense of a Zn-chlorite was instead considered as related to retrograde alteration from chlorite to smectite [43]. The textural relationship differs from that observed

for muscovite, which represents a simple template on which smectite crystallizes directly from fluids. This difference of behavior between the 10 Å- and 14 Å-phyllsilicate was considered related to the fact that chlorite is more favorably subjected to chemical alteration and weathering than white mica [43]. Even though saucnite can form under a wide range of temperatures (25–200 °C) [44], considering the present data, it is probable that the Kihabe saucnite has a supergene origin.

Among the more typical supergene phases, smithsonite is common at Kihabe in both the analyzed cores, as newly-formed crystals in cavities, but also as a direct replacement of willemite. This characteristic has been observed in many willemite-bearing nonsulfide deposits [34,45–48], and was considered as related to percolation through the soil of carbonate-rich meteoric waters, which altered the preexisting Zn-silicate. In these cases, groundwaters could have become enriched in carbonate either by leaching the host rock, or by taking organic carbon from a vegetated soil [49]. Among the Pb-minerals, cerussite was formed via a similar process, whereas the Pb-phosphates (pyromorphite and hinsdalite) formed as replacements of fluorapatite. The conversion from fluorapatite to pyromorphite is a common phenomenon in the supergene environment, resulting in an almost complete Pb → Ca and Cl → F substitution [50]. The formation of mimetite is considered to be related to the already mentioned As abundance in the Kihabe system. The described supergene mineralization is genetically related to post-Gondwana erosional episodes and the resulting supergene meteoric oxidation, spanning the period from the end of the Cretaceous to the Miocene (Figure 11; [51]).

Although not detected in the analyzed samples, the genesis of the vanadates at Kihabe can be associated with the same supergene processes that formed the Zn and Pb carbonates and phosphates (Figure 11). Vanadate deposits are widespread in the Otavi Mountainland [31], where they represent a special low-temperature, supergene-related, nonsulfide ore type [8]. The age of these vanadium ores appears to be generally confined to Cenozoic, with a distinct period of formation dated between 24 and 33 Ma [31]. The metallogenic history of V in the Aha Hills should not have been very different.

Finally, the occurrence of iodargyrite in the analyzed samples also has direct implications for the evolution of the supergene processes in the Aha Hills. In fact, the Ag-iodide is a common mineral in the supergene profiles of Au-Ag epithermal deposits occurring in arid to hyperarid areas [52], where it typically forms when the groundwaters are enriched in iodine, in response to extreme evaporation [52–55]. In the Kihabe case, the formation of iodargyrite could be related to the late stages of supergene alteration, which likely occurred during the transition from a humid to an arid climate, which has occurred since the Middle Miocene in several regions of southern Africa (Figure 11; [51,56]).

6. Conclusions

The Kihabe sulfide mineralization mainly consists of Fe-sphalerite and galena, finely disseminated in stratabound horizons within the quartzwacke, and shares several features with the ores of the Berg Aukas-type deposits (Namibia), suggesting a similar genesis. Among the nonsulfide assemblages, two mineralization types occur in the investigated samples: one characterized by hydrothermal willemite and baileychlore, and a second one instead consisting of supergene smithsonite, cerussite, Zn-Pb-phosphates, etc. Willemite is present in two generations, which should postdate sulfide emplacement, or form at their expenses. These characteristics are similar to those observed in the willemite occurrences of the Otavi Mountainland, which formed due to hydrothermal processes, during the final stages of the Damara Orogeny. The formation of the Kihabe willemite is likely coeval. Baileychlore is characterized by textures indicating direct precipitation from solutions and dissolution–crystallization mechanisms. Both processes are typical of hydrothermal systems, thus suggesting the hydrothermal genesis of the Kihabe Zn-chlorite. Baileychlore could represent an alteration halo possibly associated either with the sulfide or with willemite mineralization. The other nonsulfide minerals, smithsonite, cerussite and various Pb-phosphates, are clearly genetically associated with late phases of supergene alteration, which overprinted both the sulfide and the willemite- and baileychlore-bearing mineralizations. Supergene alteration probably occurred in this part of Botswana from the Late Cretaceous to the Miocene.

Author Contributions: Conceptualization, N.M. and M.B.; validation, N.M., G.B.; methodology and formal analysis, G.B., F.P., and L.S.; investigation, N.M., M.B., G.B.; data curation, N.M., G.B., N.F.; writing—original draft preparation, N.M., M.B.; writing—review and editing, N.M., M.B., G.B.; project administration, M.B.; funding acquisition, N.M., M.B. All authors have read and agreed to the published version of the manuscript.

Funding: The research leading to these results has received funding from the University of Naples Federico II (Italy) to M. Boni and N. Mondillo.

Acknowledgments: We would like to thank the Mt. Burgess personnel, very helpful in supplying geological information and other literature data. The authors at the University of Napoli wish to thank also R. de' Gennaro for the assistance during SEM analyses. We are grateful to G. Borg and three anonymous reviewers for comments and suggestions, which greatly enhanced the quality of the paper.

Conflicts of Interest: The authors declare no conflict of interest.

Appendix A

Table A1. Representative chemical compositions of willemite, smithsonite and cerussite (SEM-EDS).

Analyte	KDD 143-16	KDD 143-16	KDD 143-16	KDD 143-16	KDD 143-22	KDD 143-22	KDD 143-22	KDD 143-22	KDD 143-21	KDD 143-21	KDD 143-22	KDD 143-22	KDD 143-22	KDD 143-22	KDD 143-22
	Willemite	Smithsonite	Smithsonite	Smithsonite	Smithsonite	Smithsonite	Cerussite	Cerussite							
SiO ₂	25.55	26.17	25.77	26.11	26.91	26.35	26.90	26.04	n.a.						
ZnO	70.91	70.68	68.65	72.38	71.88	71.46	69.93	71.31	62.72	61.83	62.88	60.07	63.34	2.70	1.82
FeO	0.12	0.22	0.88	0.04	0.18	0.78	0.06	0.36	0.23	0.34	0.04	2.77	0.22	0.16	b.d.
MnO	0.13	0.09	0.02	b.d.	0.16	b.d.	0.18	b.d.	b.d.	0.18	b.d.	b.d.	0.06	0.14	0.29
MgO	b.d.	0.15	b.d.	b.d.	0.11	0.07	0.19	0.28	0.28	0.33	b.d.	0.38	0.42	0.14	0.15
CaO	0.06	0.17	0.10	0.01	b.d.	b.d.	0.02	0.06	0.08	b.d.	0.06	0.06	0.24	0.55	0.41
CdO	0.14	0.42	b.d.	b.d.	0.08	b.d.	0.08	b.d.	0.25	b.d.	0.32	0.67	0.40	b.d.	b.d.
PbO	b.d.	0.03	0.16	0.18	b.d.	0.21	1.51	0.26	0.30	0.07	0.21	0.16	0.46	78.47	78.33
BaO	n.a.	0.24	0.15												
As ₂ O ₅	2.87	2.18	2.43	1.91	1.35	1.90	0.52	2.02	0.58	0.78	0.72	0.13	0.29	b.d.	b.d.
CO ₂ *									34.85	34.50	34.57	34.97	35.42	17.78	17.14
Total	99.78	100.12	98.00	100.64	100.66	100.76	99.40	100.33	99.29	98.04	98.80	99.22	100.83	100.19	98.28

n.a., not analyzed; b.d., below detection limit; * CO₂ by stoichiometry.

Table A2. Chemical compositions (SEM-EDS) and structural formulae (in atoms per formula units, apfu) of baileychlore from the KDD 143 core. The number of cations are calculated on the basis of O₁₀(OH)₈.

Analyte	Rule and Radke (1988)	KDD 143-21	KDD 143-22	KDD 143-21	KDD 143-22	KDD 143-22	KDD 143-24	KDD143-24	KDD 143-26	KDD 143-26							
		Site 5 Spectrum 3	Site 5 Spectrum 1	Site 7 Spectrum 3	Site 2 Spectrum 3	Site 3 Spectrum 2	Site 12 Spectrum 1	Site 12 Spectrum 2	Site 1 Spectrum 3	Site 4 Spectrum 8	Site 4 Spectrum 4	Site 7 Spectrum 1	Site 7 Spectrum 2	Site 5 Spectrum 2	Site 5 Spectrum 2	Site 10 Spectrum 4	Site 1 Spectrum 3
SiO ₂	32.00	28.48	29.09	30.00	31.41	31.30	29.68	29.88	30.74	30.48	29.52	30.28	27.55	31.32	30.91	26.68	26.06
TiO ₂		0.01		0.07	0.09	0.13	–	0.08	0.12	–	0.36	0.32	0.14	–	–	–	–
Al ₂ O ₃	12.40	10.97	11.55	10.27	12.91	12.89	11.35	11.66	15.31	15.15	14.14	16.05	13.84	14.19	15.42	13.57	14.24
FeO	12.90	0.51	0.65	0.15	0.31	1.10	1.29	1.60	1.62	1.01	0.87	1.15	0.79	1.36	1.76	1.64	0.79
MnO	0.15	–	0.11	0.04	–	0.17	0.25	0.14	0.12	0.04	0.18	0.13	–	0.03	–	0.06	–
MgO	4.60	1.84	1.95	1.69	2.09	1.68	2.14	2.32	1.96	1.90	1.70	2.44	3.57	1.76	2.09	2.19	1.52
CaO	1.00	0.35	0.42	0.64	0.57	0.64	0.65	0.59	0.45	0.51	0.55	0.42	0.38	0.58	0.31	0.36	0.27
ZnO	30.50	47.64	46.26	46.02	45.26	41.58	43.22	43.76	40.65	42.04	41.71	41.70	41.57	37.47	38.91	43.42	44.38
CuO	–	–	–	–	–	–	0.12	–	1.10	1.40	1.13	0.90	0.88	1.54	0.72	0.55	0.50
Total apfu	93.55	89.80	90.03	88.88	92.64	89.49	88.70	90.02	92.06	92.53	90.16	93.40	88.72	88.25	90.12	88.46	87.76
		tetrahedral cations (Σ = 4)															
Si	3.52	3.46	3.49	3.63	3.57	3.64	3.56	3.53	3.46	3.44	3.44	3.36	3.28	3.62	3.51	3.25	3.21
Al ^{IV}	0.48	0.54	0.51	0.37	0.43	0.36	0.44	0.47	0.54	0.56	0.56	0.64	0.72	0.38	0.49	0.75	0.79
Al ^{VI}	1.13	1.04	1.12	1.10	1.30	1.40	1.17	1.16	1.49	1.45	1.38	1.46	1.23	1.56	1.57	1.20	1.28
Ti	0.00	0.00	0.00	0.01	0.01	0.01	0.00	0.01	0.01	0.00	0.03	0.03	0.01	0.00	0.00	0.00	0.00
Fe ²⁺	1.19	0.05	0.07	0.02	0.03	0.11	0.13	0.16	0.15	0.10	0.08	0.11	0.08	0.13	0.17	0.17	0.08
Mn	0.01	0.00	0.01	0.00	0.00	0.02	0.03	0.01	0.01	0.00	0.02	0.01	0.00	0.00	0.01	0.01	0.00
Mg	0.75	0.33	0.35	0.30	0.35	0.29	0.38	0.41	0.33	0.32	0.29	0.40	0.63	0.30	0.35	0.40	0.28
Ca	0.12	0.05	0.05	0.08	0.07	0.08	0.08	0.08	0.05	0.06	0.07	0.05	0.05	0.07	0.04	0.05	0.04
Zn	2.48	4.28	4.10	4.11	3.80	3.57	3.83	3.82	3.38	3.50	3.59	3.42	3.66	3.20	3.26	3.91	4.04
Cu	0.00	0.00	0.00	0.00	0.00	0.00	0.12	0.00	1.10	1.40	1.13	0.90	0.88	1.54	0.72	0.55	0.50
Sum Oct.	5.68	5.75	5.70	5.62	5.56	5.48	5.74	5.65	6.52	6.83	6.59	6.38	6.54	6.80	6.11	6.29	6.22
R ²⁺	4.55	4.71	4.58	4.51	4.25	4.07	4.57	4.48	5.02	5.38	5.18	4.89	5.30	5.24	4.54	5.09	4.94

–, not detected.

Table A3. Representative chemical composition (SEM-EDS) of miscellaneous minerals detected in the Kihabe nonsulfide associations.

Analyte	KDD 143-24	KDD 143-24	KDD 143-24	KDD 143-26	KDD 143-26	KDD 143-26	KDD 143-26	KDD 143-26	KDD 143-22	KDD 143-22	KDD 143-22	KDD 143-22	KDD 143-22	KDD 143-22
	Mimetite	Mimetite	Mimetite	Pyromorphite	Pyromorphite	Hinsdalite	Hinsdalite	Hinsdalite	Fe-Oxy- hydroxides	Fe-Oxy- hydroxides	Fe-Oxy- hydroxides	Fe-Oxy- hydroxides	Fe-Oxy- hydroxides	Fe-Oxy- hydroxides
Al ₂ O ₃	n.a.	n.a.	n.a.	n.a.	n.a.	16.45	19.78	16.59	0.52	1.04	1.50	1.24	0.20	0.65
Fe ₂ O ₃	n.a.	n.a.	n.a.	n.a.	n.a.	5.64	1.28	4.20	95.98	91.49	91.30	87.22	81.00	74.52
ZnO	b.d.	0.50	b.d.	0.35	0.76	2.18	2.75	1.73	1.78	1.15	1.96	2.89	1.99	4.98
FeO	b.d.	b.d.	2.85	0.06	0.31	5.13	1.17	3.82	n.a.	n.a.	n.a.	n.a.	n.a.	n.a.
MnO	0.22	b.d.	b.d.	0.28	0.06	b.d.	b.d.	b.d.	b.d.	0.20	b.d.	b.d.	b.d.	0.01
MgO	b.d.	b.d.	b.d.	0.11	b.d.	b.d.	0.16	b.d.	b.d.	0.39	0.14	b.d.	0.05	0.11
CaO	0.03	0.35	0.31	2.08	1.15	0.63	0.22	0.13	0.05	b.d.	0.05	b.d.	0.25	0.19
CdO	0.32	0.24	0.03	b.d.	0.20	b.d.	b.d.	0.18	b.d.	0.29	0.13	0.86	b.d.	0.02
PbO	74.57	73.23	74.47	78.46	80.47	45.98	38.22	42.21	1.02	3.13	1.65	1.36	5.61	2.89
SrO	b.d.	b.d.	b.d.	0.92	0.81	0.35	0.38	0.28	b.d.	0.81	0.40	0.08	0.28	0.20
BaO	0.11	0.04	0.41	0.46	b.d.	0.74	0.18	b.d.	b.d.	0.15	0.12	0.25	b.d.	b.d.
As ₂ O ₅	22.08	21.22	21.95	b.d.	0.26	1.40	1.50	1.97	0.57	0.60	0.01	1.93	2.00	b.d.
P ₂ O ₅	0.44	0.53	0.27	16.19	15.27	11.38	10.04	9.35	n.a.	n.a.	n.a.	n.a.	n.a.	n.a.
Cl	2.46	2.62	3.32	2.93	2.91	0.50	0.10	0.38	n.a.	n.a.	n.a.	n.a.	n.a.	n.a.
SO ₃	n.a.	n.a.	n.a.	n.a.	n.a.	9.42	9.78	8.86	n.a.	n.a.	n.a.	n.a.	n.a.	n.a.
Total	100.23	98.73	103.63	101.83	102.18	99.78	85.54	89.70	99.92	98.43	97.26	95.83	91.38	83.56

n.a., not analyzed; b.d., below detection limit.

Table A4. Chemical analyses (wt. %) of selected Kihabe samples (ICP-ES-MS).

Analyte	Sample #	KDD 125-2	KDD 125-4	KDD 125-5	KDD 125-7	KDD 125-8	KDD 125-9	KDD 125-10	KDD 125-12	KDD 125-14	KDD 143-16	KDD 143-18	KDD 143-20	KDD 143-21	KDD 143-22	KDD 143-23	KDD 143-24	KDD 143-25	KDD 143-26	KDD 143-27	KDD 143-29	
wt. %	Det. Lim.																					
SiO ₂	0.01	81.03	76.58	76.6	79.17	77.47	80.65	81.44	82.05	82.15	81.97	74.09	79.8	75.41	76.63	67.85	72.35	75.59	76.26	83.27	78.04	
Ti	0.001	0.08	0.09	0.08	0.12	0.09	0.09	0.14	0.13	0.06	0.07	0.24	0.07	0.08	0.10	0.09	0.08	0.06	0.09	0.11	0.07	
Al	0.01	4.26	3.57	4.38	4.64	3.51	3.54	3.75	4.70	4.03	3.30	3.85	3.92	3.71	3.20	3.27	3.26	3.43	3.18	3.95	3.60	
Fe	0.01	0.76	1.07	2.20	0.62	0.84	0.72	1.38	1.11	0.51	0.61	0.92	0.59	0.69	0.76	0.82	0.96	0.66	0.64	0.57	0.47	
Mg	0.01	0.10	0.09	0.10	0.12	0.10	0.09	0.10	0.13	0.11	0.19	0.27	0.19	0.21	0.15	0.22	0.18	0.24	0.26	0.17	0.14	
Ca	0.01	0.02	0.02	0.01	0.02	0.02	0.02	0.02	0.01	b.d.	0.04	0.10	0.05	0.05	0.05	0.05	0.06	0.08	0.11	0.09	0.10	
Na	0.01	b.d.	0.03	0.03	0.03	0.03	0.03	0.03	0.03	0.03	0.02	b.d.	0.03	0.03	0.02	0.02	0.06	0.08	0.07	0.08	0.06	
K	0.01	2.30	2.07	2.37	2.54	2.03	2.14	2.13	2.67	2.55	1.86	2.33	2.29	2.15	1.83	1.81	1.75	2.09	1.61	2.54	1.86	
P	0.01	0.02	0.03	0.02	0.02	0.02	0.02	0.02	0.02	0.02	0.02	0.04	0.02	0.02	0.03	0.03	0.03	0.03	0.03	0.03	0.02	
S	0.05	0.44	2.42	1.71	0.07	1.45	1.78	1.80	0.06	b.d.	0.19											
Zn	0.0005	0.03	4.30	3.08	0.19	4.28	3.09	1.40	0.07	0.53	3.37	4.91	3.49	6.04	5.12	9.32	7.06	4.66	5.24	0.96	1.47	
Pb	0.0005	2.61	1.94	0.96	3.09	1.38	1.05	0.48	0.20	1.80	0.33	1.02	0.57	0.26	2.04	2.02	1.30	2.56	1.82	0.54	4.82	
mg/kg																						
Li	0.5	6.8	5.8	5.7	9.9	5.8	6.7	5.9	8	6.8	15.4	10.9	7.5	7.9	9.5	10.2	11	7.2	6.9	9.7	8.9	
V	10	21	19	24	31	23	15	20	29	16	16	51	18	58	262	23	27	19	20	28	20	
Cr	1	60	14	91	13	65	10	87	12	51	12	84	10	72	18	66	9	54	14	63	7	
Mn	5	39	58	45	42	51	44	40	34	33	45	45	42	42	46	47	52	39	35	38	40	
Co	1	b.d.	2	2	b.d.	4	5	7	b.d.	b.d.	2	9	8	10	8	25	18	32	31	5	3	
Ni	0.5	3	4.9	6.8	1.1	7.3	8.6	15.7	b.d.	2.8	3.8	21.1	10.9	13.3	8.9	20	11.3	12.6	12.3	7.5	2.1	
Cu	0.5	49.9	20.7	15.2	33.8	103.8	9.1	6.7	4.2	62.4	66.1	204.5	176.6	424.1	794.6	1831.5	1394.2	973.7	1131.5	477.1	1365.7	
As	5	294	256	182	406	419	29	41	64	134	275	76	72	81	117	3647	2007	172	119	39	42	
Rb	0.5	81.5	75.5	85.9	94.9	74	75.1	80.1	105.3	97.3	72.5	92.1	85.7	81.3	70.3	67.7	69.3	73.3	54.5	91.7	76.8	
Sr	5	46	10	7	8	7	5	6	7	20	5	8	10	7	13	7	6	31	28	13	28	
Y	0.5	2.5	2.9	2.8	4.3	25	8.7	10.3	11.6	6.5	5.9	9.7	6.7	6.3	6.6	6.2	6.3	6.6	6.8	7.2	6.9	
Zr	0.5	52.7	48.9	48.3	62.1	48.5	45.6	72.5	66.6	43.9	41.6	113.8	46.3	44.7	48.4	44.6	40	48.7	50.1	49.7	44.2	
Nb	0.5	3.5	3.1	3.1	4.5	3.1	3.8	5.2	4.5	3	3.3	8.9	3	3.4	3.9	3.1	3	2.3	3.6	4.2	3.1	
Mo	0.5	1.4	1.4	1.6	1.5	1.4	1.3	1.4	1.8	1.1	1.4	1	2.2	2.1	3.7	11.9	2.8	2	2.3	1.5	4.4	
Ag	0.5	50.3	38.8	20.7	99.8	39.3	12.1	7.8	27.2	27.7	17.6	49.2	15.9	17.8	47.3	39.8	39	103.1	112	27.7	102.8	
Cd	0.5	0.5	200.7	100.9	6.4	114.2	271.4	69.8	6.5	35	50.7	144.7	86.6	186.9	131.4	410.2	417.8	7.8	10.2	1.4	2177.5	
Sb	0.5	1.2	1.2	1.6	1.2	0.9	0.8	b.d.	1.2	0.5	3.6	2.6	1.5	4.2	9.1	28.3	24.6	5.7	5.7	2.6	12.2	
Ba	5	140	92	112	153	109	97	100	146	307	166	218	205	204	188	183	165	347	1232	253	957	
La	0.5	21.9	19.8	20.6	29.7	24.8	24.8	27.4	28.1	24.2	12.9	27.7	23.9	22	15.7	14.7	15.3	17.7	13.8	19.5	18.1	
Ce	5	43	39	41	61	49	48	56	53	47	27	54	46	42	29	29	29	36	28	37	35	
Hf	0.5	1.6	1.5	1.4	1.4	1.5	1.4	2.2	1.8	1.3	1.3	3.2	1.4	1.4	1.3	1.1	1	1.2	1.5	1.1	1	
Th	0.5	5.1	5.9	6.2	7.4	5.5	5.6	10.2	7.5	4.2	4.1	16.9	4.6	4.7	8.2	6.2	5.1	4.1	7	6.6	4.8	
U	0.5	2	3.2	2.7	5.5	4.7	1.3	1.7	1.8	1.9	0.8	1.9	1	1.1	1.8	2.6	2.1	1.6	1.3	1.2	1.3	

b.d., below detection limit.

References

1. Botswana Geoscience Institute. Botswana Mineral Projects and Prospects. Ministry of Mineral Resources, Green Technology and Energy Security. 2020, p. 28. Available online: <http://www.bgi.org.bw/sites/default/files/Brochure%20on%20Botswana%20Mineral%20Projects%20and%20Prospects%202020%20Version.pdf> (accessed on 1 July 2020).
2. Cairncross, B. The Otavi Mountain Land Cu-Pb-Zn-V Deposits. *Mineral. Rec.* **1997**, *28*, 109–130.
3. Melcher, F.; Oberthür, T.; Rammelmair, D. Geochemical and mineralogical distribution of germanium in the Khusib Springs Cu-Zn-Pb-Ag sulfide deposit, Otavi Mountain Land, Namibia. *Ore Geol. Rev.* **2006**, *28*, 32–56. [[CrossRef](#)]
4. Pirajno, F.; Joubert, B.D. An overview of carbonate-hosted mineral deposits in the Otavi mountain land, Namibia; implications for ore genesis. *J. Afr. Earth Sci.* **1993**, *16*, 265–272. [[CrossRef](#)]
5. Chetty, D.; Frimmel, H.E. The role of evaporites in the genesis of base metal sulphide mineralisation in the northern platform of the Pan-African Damara Belt, Namibia; geochemical and fluid inclusion evidence from carbonate wall rock alteration. *Mineral. Depos.* **2000**, *35*, 364–376. [[CrossRef](#)]
6. Hughes, M.J. The Tsumeb Ore Body, Namibia, and Related Dolostone-Hosted Base Metal Ore Deposits of Central Africa. Ph.D. Thesis, University of the Witwatersrand, Johannesburg, South Africa, 1987; p. 473.
7. Hitzman, M.W.; Reynolds, N.A.; Sangster, D.F.; Allen, C.R.; Carman, C.E. Classification, genesis, and exploration guides for nonsulfide Zinc deposits. *Econ. Geol.* **2003**, *98*, 685–714. [[CrossRef](#)]
8. Boni, M.; Mondillo, N. The “Calamines” and the “Others”: The great family of supergene nonsulfide zinc ores. *Ore Geol. Rev.* **2015**, *67*, 208–233. [[CrossRef](#)]
9. Melcher, F. The Otavi Mountain Land in Namibia: Tsumeb, Germanium and Snowball Earth. *Mitt. Österr. Miner. Ges.* **2003**, *148*, 413–435.
10. Mondillo, N.; Accardo, M.; Boni, M.; Boyce, A.; Herrington, R.; Rumsey, M.; Wilkinson, C. New insights into the genesis of willemite (Zn₂SiO₄) from zinc nonsulfide deposits, through trace elements and oxygen isotope geochemistry. *Ore Geol. Rev.* **2020**, *118*, 103307. [[CrossRef](#)]
11. Mount Burgess Mining N.L. Available online: <http://www.mountburgess.com> (accessed on 1 July 2020).
12. Carney, J.N.; Aldiss, D.T.; Lock, N.P. The geology of Botswana. *Botsw. Geol. S. Bull.* **1994**, *37*, 113.
13. Key, R.; Ayers, N. The 1998 Edition of the Geological Map of Botswana. *J. Afr. Earth Sci.* **2000**, *30*, 427–451. [[CrossRef](#)]
14. Lehmann, J.; Master, S.; Milani, L.; Kinnaird, J.A.; Naydenov, K.V.; Kumar, S.M. Regional aeromagnetic and stratigraphic correlations of the Kalahari Copperbelt in Namibia and Botswana. *Ore Geol. Rev.* **2015**, *71*, 169–190. [[CrossRef](#)]
15. Mapeo, R.B.M.; Wendorff, M.; Ramokate, L.V.; Armstrong, R.A.; Mphinyane, T.; Koobokile, M. Zircon geochronology of basement granitoid gneisses and sedimentary rocks of the Tsodilo Hills Group in the Pan-African Damara Belt, western Botswana: Age constraints, provenance, and tectonic significance. *J. Afr. Earth Sci.* **2019**, *159*, 103576. [[CrossRef](#)]
16. Meixner, H.M.; Peart, R.J. The Kalahari Drilling Project. *Botsw. Geol. S. Bull.* **1984**, *27*, 224.
17. Singletary, S.J.; Hanson, R.E.; Martin, M.W.; Crowley, J.L.; Bowring, S.A.; Key, R.M.; Ramokate, L.V.; Direng, B.B.; Krol, M.A. Geochronology of basement rocks in the Kalahari Desert, Botswana, and implications for regional Proterozoic tectonics. *Precambrian Res.* **2003**, *121*, 47–71. [[CrossRef](#)]
18. Wendorff, M. Outline of lithostratigraphy sedimentation and tectonics of the Tsodilo Hills Group, Neoproterozoic Lower Paleozoic siliciclastic succession in NW Botswana. *Ann. Soc. Geol. Pol.* **2005**, *75*, 17–25.
19. Killick, A.M. A preliminary account of the geology of the Kamtsas Formation of the Damara Sequence, eastern Gobabis District, South West Africa/Namibia. *Trans. Geol. Soc. S. Afr.* **1983**, *86*, 11–18.
20. Hoffman, K.H. New aspects of lithostratigraphic subdivision and correlation of Late Proterozoic to Early Cambrian rocks of the southern Damara Belt and their correlation with the central and northern Damara Belt and the Gariiep belt. *Namib. Geol. Surv. Commun.* **1989**, *5*, 59–67.
21. Schwartz, M.O.; Kwok, Y.Y.; Davis, D.W.; Akangyang, P. Geology, geochronology and regional correlation of the Ghanzi Ridge, Botswana. *S. Afr. J. Geol.* **1996**, *99*, 245–250.
22. Hanson, R.E. Proterozoic geochronology and tectonic evolution of southern Africa. *Geol. Soc. Lond. Spec. Publ.* **2003**, *206*, 427–463. [[CrossRef](#)]

23. Reeves, C.V. *Reconnaissance Aeromagnetic Survey of Botswana, 1975–1977*; Final interpretation report; Terra Surveys Ltd., Botswana Geological Survey: Lobatse, Botswana, 1978.
24. Chatupa, J.C.; Direng, B.B. Distribution of trace and major elements in the-180 + 75 μm and -75 μm fractions of the Sandveld regolith in northwest Ngamiland, Botswana. *J. Afr. Earth Sci.* **2000**, *30*, 515–534. [[CrossRef](#)]
25. Loxton, R.F. *A Photogeological Study of the Aha Hills, Northwest Botswana*; Loxton, Hunting and Associates, Report for Billiton Botswana (Pty) Ltd.: Gaborone, Botswana, 1981; p. 27.
26. Stalker, A.D. *Aha Hills Prospecting Licence 39180*; Final Report; Billiton Botswana (Pty) Limited: Gaborone, Botswana, 1983; p. 13.
27. Mapeo, R.B. *Geological and Structural Analysis of the Kihabe Base Metal Prospect in NW Botswana*; Internal Report for Mount Burgess (Botswana) (Pty) Ltd.: Gaborone, Botswana, 2007; p. 41.
28. Rule, A.C.; Radke, F. Baileychlore, the Zn end member of the trioctahedral chlorite series. *Am. Mineral.* **1988**, *73*, 135–139.
29. Gray, D.R.; Foster, D.A.; Goscombe, B.; Passchier, C.W.; Trouw, R.A.J. $^{40}\text{Ar}/^{39}\text{Ar}$ thermochronology of the Pan-African Damara Orogen, Namibia, with implications for tectonothermal and geodynamic evolution. *Prec. Res.* **2006**, *150*, 49–72. [[CrossRef](#)]
30. Schneider, J.; Boni, M.; Laukamp, C.; Bechstadt, T.; Petzel, V. Willemite (Zn_2SiO_4) as a possible Rb–Sr geochronometer for dating nonsulfide Zn–Pb mineralization: Examples from the Otavi Mountainland (Namibia). *Ore Geol. Rev.* **2008**, *33*, 152–167. [[CrossRef](#)]
31. Boni, M.; Terracciano, R.; Evans, N.; Laukamp, C.; Schneider, J.; Bechstadt, T. Genesis of vanadium ore in Otavi Mountainland, Namibia. *Econ. Geol.* **2007**, *102*, 441–469. [[CrossRef](#)]
32. Brugger, J.; McPhail, D.C.; Wallace, M.; Waters, J. Formation of Willemite in Hydrothermal Environments. *Econ. Geol.* **2003**, *98*, 819–835. [[CrossRef](#)]
33. Kamona, A.F.; Friedrich, G.H. Geology, mineralogy and stable isotope geochemistry of the Kabwe carbonate-hosted Pb–Zn deposit, Central Zambia. *Ore Geol. Rev.* **2007**, *30*, 217–243. [[CrossRef](#)]
34. Mondillo, N.; Herrington, R.; Boyce, A.J.; Wilkinson, C.; Santoro, L.; Rumsey, M. Critical elements in non-sulfide Zn deposits: A reanalysis of the Kabwe Zn–Pb ores (central Zambia). *Mineral. Mag.* **2018**, *82*, S89–S114. [[CrossRef](#)]
35. White, A.J.R.; Pearce, M.A.; Meadows, H.R. Distinguishing regional- and local-scale metasomatic systems at the Prairie Downs Zn–Pb deposit. *Lithos* **2016**, *262*, 247–265. [[CrossRef](#)]
36. Galley, A.G.; Hannington, M.D.; Jonasson, I.R. Mineral Deposits of Canada: A Synthesis of Major Deposit-Types, District Metallogeny, the Evolution of Geological Provinces, and Exploration Methods. In *Geological Association of Canada, Mineral Deposits Division, Special Publication No. 5*; Goodfellow, W.D., Ed.; Geological Association of Canada, Mineral Deposits Division: St. John’s, NL, Canada, 2007; pp. 141–161.
37. Spry, P.G.; Peter, J.M.; Slack, J.F. Meta-exhalites as exploration guides to ore. In *Metamorphosed and Metamorphogenic Ore Deposits*; Reviews in Economic Geology; Spry, P.G., Marshall, B., Vokes, F.M., Eds.; Society of Economic Geologists: Littleton, CO, USA, 2000; Volume 11, pp. 163–201.
38. Beaufort, D.; Rigault, C.; Billon, S.; Billault, V.; Inoue, A.; Inoue, S.; Patrier, P. Chlorite and chloritization processes through mixed-layer mineral series in lowtemperature geological systems—A review. *Clay Miner.* **2015**, *50*, 497–523. [[CrossRef](#)]
39. Abad, I.; Jimenez-Millan, J.; Sanchez-Roa, C.; Nieto, F.; Velilla, N. Neocrystallization of clay minerals in the Alhama de Murcia Fault (southeast Spain): Implications for fault mechanics. *Clay Miner.* **2019**, *54*, 1–13. [[CrossRef](#)]
40. Do Campo, M.; Bauluz, B.; Nieto, F.; Papa, C.; Hongn, F. SEM and TEM evidence of mixed-layer illite-smectite formed by dissolution crystallization processes in continental Paleogene sequences in northwestern Argentina. *Clay Miner.* **2016**, *51*, 723–740. [[CrossRef](#)]
41. Bourdelle, F.; Cathelineau, M. Low-temperature chlorite geothermometry: A graphical representation based on a T–R²⁺–Si diagram. *Eur. J. Mineral.* **2015**, *27*, 617–626. [[CrossRef](#)]
42. Pacey, A.; Wilkinson, J.J.; Cooke, D.R. Chlorite and epidote mineral chemistry in porphyry ore systems: A case study of the Northparkes District, New South Wales, Australia. *Econ. Geol.* **2020**, *115*, 701–727. [[CrossRef](#)]
43. Balassone, G.; Nieto, F.; Arfe, G.; Boni, M.; Mondillo, N. Zn-clay minerals in the Skorpion Zn nonsulfide deposit (Namibia): Identification and genetic clues revealed by HRTEM and AEM study. *Appl. Clay Sci.* **2017**, *150*, 309–322. [[CrossRef](#)]

44. Mondillo, N.; Nieto, F.; Balassone, G. Micro and nano-characterization of Zn-clays in nonsulfide supergene ores of southern Peru. *Am. Mineral.* **2015**, *100*, 2484–2496. [[CrossRef](#)]
45. Choulet, F.; Charles, N.; Barbanson, L.; Branquet, Y.; Sizaret, S.; Ennaciri, A.; Badra, L.; Chen, Y. Non-sulfide zinc deposits of the moroccan high atlas: Multi-scale characterization and origin. *Ore Geol. Rev.* **2014**, *56*, 115–140. [[CrossRef](#)]
46. Choulet, F.; Richard, J.; Boiron, M.-C.; Dekoninck, A.; Yans, J. Distribution of trace elements in willemite from the Belgium non-sulphide deposits. *Eur. J. Mineral.* **2019**, *31*, 983–997. [[CrossRef](#)]
47. Coppola, V.; Boni, M.; Gilg, H.A.; Balassone, G.; Dejonghe, L. The “calamine” nonsulfide Zn–Pb deposits of Belgium: Petrographical, mineralogical and geochemical characterization. *Ore Geol. Rev.* **2008**, *33*, 187–210. [[CrossRef](#)]
48. Monteiro, L.V.S.; Bettencourt, J.S.; Juliani, C.; de Oliveira, T.F. Geology, petrography, and mineral chemistry of the Vazante non-sulfide and Ambrósia and Fagundes sulfide-rich carbonate-hosted Zn-(Pb) deposits, Minas Gerais. Brazil. *Ore Geol. Rev.* **2006**, *28*, 201–234. [[CrossRef](#)]
49. Gilg, H.A.; Boni, M.; Hochleitner, R.; Struck, U. Stable isotope geochemistry of carbonate minerals in supergene oxidation zones of Zn–Pb deposits. *Ore Geol. Rev.* **2008**, *33*, 117–133. [[CrossRef](#)]
50. Markl, G.; Marks, M.A.W.; Holzäpfel, J.; Wenzel, T. Major, minor, and trace element composition of pyromorphite-group minerals as recorder of supergene weathering processes from the Schwarzwald mining district, SW Germany. *Am. Mineral.* **2014**, *99*, 1133–1146. [[CrossRef](#)]
51. Partridge, T.C.; Maud, R.R. Geomorphic evolution of southern Africa since the Mesozoic. *S. Afr. J. Geol.* **1987**, *90*, 179–208.
52. Sillitoe, R.H. Supergene silver enrichment reassessed. In *Supergene environments, processes, and products. Soc. Econ. Geol. Spec. Publ.* **2009**, *14*, 15–32.
53. Boyle, D.R. Iodargyrite as an indicator of arid climatic conditions and its association with gold-bearing glacial tills of the Chibougamau–Chapais area, Quebec. *Can. Mineral.* **1997**, *35*, 23–34.
54. Gammons, C.H.; Yu, Y. The stability of aqueous silver bromide and iodine complexes at 25–300 °C. Experiments, theory and geologic applications. *Chem. Geol.* **1997**, *137*, 155–173. [[CrossRef](#)]
55. Golebiowska, B.; Pieczka, A.; Rzepa, G.; Matyszkiewicz, J.; Krajewski, M. Iodargyrite from Zalas (Cracow area, Poland) as an indicator of Oligocene–Miocene aridity in Central Europe. *Palaeogeogr. Palaeoclimatol. Palaeoecol.* **2010**, *296*, 130–137. [[CrossRef](#)]
56. Van der Wateren, F.M.; Dunai, T.G. Late Neogene passive margin denudation history—Cosmogenic isotope measurements from the central Namib desert. *Glob. Planet. Chang.* **2001**, *30*, 271–307. [[CrossRef](#)]



© 2020 by the authors. Licensee MDPI, Basel, Switzerland. This article is an open access article distributed under the terms and conditions of the Creative Commons Attribution (CC BY) license (<http://creativecommons.org/licenses/by/4.0/>).